Chemical Science

ROYAL SOCIETY OF CHEMISTRY

REVIEW

View Article Online
View Journal | View Issue

Check for updates

Cite this: *Chem. Sci.*, 2024, **15**, 5869

# Rare-earth-based chalcogenides and their derivatives: an encouraging IR nonlinear optical material candidate

Ping Feng,†[abcd] Jia-Xiang Zhang,†[abe] Mao-Yin Ran,[abe] Xin-Tao Wu,[abd] Hua Lin *[abd] and Qi-Long Zhu *[abdf]

With the continuous development of laser technology and the increasing demand for lasers of different frequencies in the infrared (IR) spectrum, research on infrared nonlinear optical (NLO) crystals has garnered growing attention. Currently, the three main commercially available types of borate materials each have their drawbacks, which limit their applications in various areas. Rare-earth (RE)-based chalcogenide compounds, characterized by the unique f-electron configuration, strong positive charges, and high coordination numbers of RE cations, often exhibit distinctive optical responses. In the field of IR-NLO crystals, they have a research history spanning several decades, with increasing interest. However, there is currently no comprehensive review summarizing and analyzing these promising compounds. In this review, we categorize 85 representative examples out of more than 400 non-centrosymmetric (NCS) compounds into four classes based on the connection of different asymmetric building motifs: (1) RE-based chalcogenides containing tetrahedral motifs; (2) RE-based chalcogenides containing lone-pair-electron motifs; (3) RE-based chalcogenides containing [$BS_3$] and [$P_2Q_6$] motifs; and (4) RE-based chalcohalides and oxychalcogenides. We provide detailed discussions on their synthesis methods, structures, optical properties, and structure–performance relationships. Finally, we present several favorable suggestions to further explore RE-based chalcogenide compounds. These suggestions aim to approach these compounds from a new perspective in the field of structural chemistry and potentially uncover hidden treasures within the extensive accumulation of previous research.

Received 30th January 2024
Accepted 3rd March 2024

DOI: 10.1039/d4sc00697f

rsc.li/chemical-science

Open Access Article. Published on 22 2024. Downloaded on 18/10/24 08:09:28.
This article is licensed under a Creative Commons Attribution 3.0 Unported Licence.

[a]*State Key Laboratory of Structural Chemistry, Fujian Institute of Research on the Structure of Matter, Chinese Academy of Sciences, Fuzhou, Fujian 350002, China. E-mail: linhua@fjirsm.ac.cn; qlzhu@fjirsm.ac.cn*

[b]*Fujian Science & Technology Innovation Laboratory for Optoelectronic Information of China, Fujian 350108, China*

[c]*College of Chemistry, Fuzhou University, Fuzhou 350002, China*

[d]*Fujian College, University of Chinese Academy of Sciences, Fuzhou 350002, China*

[e]*University of Chinese Academy of Sciences, Beijing 100049, China*

[f]*Fujian Key Laboratory of Rare-earth Functional Materials, Fujian Shanhai Collaborative Innovation Center of Rare-earth Functional Materials, Longyan 366300, China*

† These authors contributed equally to this work.

**Ping Feng**

*Ping Feng is a joint graduate student at Fujian Institute of Research on the Structure of Matter (FJIRSM) and Fuzhou University (FZU). Her research interests focus on the design and synthesis of RE-based nonlinear optical (NLO) materials for infrared (IR) applications.*

**Jia-Xiang Zhang**

*Jia-Xiang Zhang is a M.S. candidate at Fujian Institute of Research on the Structure of Matter (FJIRSM), Chinese Academy of Sciences (CAS). His research interests focus on the design, synthesis, theory, and structure–property relationships of infrared nonlinear optical (IR NLO) crystals.*

© 2024 The Author(s). Published by the Royal Society of Chemistry

Open Access Article. Published on 22 2024. Downloaded on 18/10/24 08:09:28.
This article is licensed under a Creative Commons Attribution 3.0 Unported Licence.

## 1. Introduction

The laser, an acronym for "Light Amplification by Stimulated Emission of Radiation," has found extensive applications in the military, technology, medical, and industrial production sectors. The outstanding features of lasers, including excellent collimation, monochromaticity, coherence, and high brightness, make them an indispensable tool.[1–5] However, these advantages of lasers also pose limitations to their development. The generation mechanism of lasers dictates that their wavelength is constrained. Second harmonic generation (SHG), which is a nonlinear optical (NLO) effect, enables the expansion of the working wavelengths for lasers.[6–20] Extensive research has been carried out in the ultraviolet-visible (UV-vis) spectrum over the past few decades, with a focus on inorganic crystals known for their stability and significant effective frequency-doubling coefficient ($d_{eff}$). Crystals such as $KH_2PO_4$ (KDP),[21] $KTiOPO_4$ (KTP),[22] $LiB_3O_5$ (LBO),[23] and β-$BaB_2O_4$ (β-BBO)[24] have been discovered and boast excellent properties.

Due to the evolving demands of laser technology, the UV-vis spectrum is no longer sufficient. This has led to a need for research into longer and shorter wavelengths. The study of NLO crystals in the infrared (IR) and deep ultraviolet (DUV) ranges has become crucial in laser technology. Currently, the commercially available IR-NLO crystals primarily consist of $AgGaS_2$,[25] $AgGaSe_2$,[26] and $ZnGeP_2$.[27] However, they all have some unavoidable drawbacks. For instance, $AgGaS_2$ and $AgGaSe_2$ both have a low laser-induced damage threshold (LIDT) and $AgGaSe_2$ is non-phase-matching (NPM) at 1064 nm. Additionally, $ZnGeP_2$ exhibits unfavourable multi-photon absorption. Therefore, there is an urgent demand for superior commercial large crystals, which has prompted research into outstanding candidates for IR-NLO crystals. The traditional method of exploring new IR-NLO crystals involves using powder sample tests to evaluate performance instead of waiting for large-size single crystals. However, this traditional experiment is time consuming. Nowadays, new theoretical calculation techniques are often used to deepen the knowledge of the structure–performance relationship and aid in design, even using

**Mao-Yin Ran**

*Mao-Yin Ran is a PhD candidate at Fujian Institute of Research on the Structure of Matter (FJIRSM), Chinese Academy of Sciences (CAS). He received his Master's degree at Fuzhou University (FZU). His research interest is exploring new heteroanionic nonlinear optical (NLO) materials.*

**Hua Lin**

*Hua Lin is a professor at Fujian Institute of Research on the Structure of Matter (FJIRSM), Chinese Academy of Sciences (CAS). He received his PhD degree in Physical Chemistry from FJIRSM-CAS in 2012 and joined Prof. Qi-Long Zhu's group in 2017. He has published more than 120 papers in refereed journals. His research interest currently focuses on the design, synthesis, characterization, and structure–property relationships of thermoelectric (TE) materials and infrared nonlinear optical (IR NLO) crystals.*

**Xin-Tao Wu**

*Xin-Tao Wu is an Academician of Chinese Academy of Sciences. He has published more than 400 peer-reviewed SCI papers and was recognized as the most-cited Chinese author by Elsevier for five consecutive years (2014–2018). He is mainly engaged in structural chemistry and cluster chemistry and has made leading achievements in the fields of sulfur-containing cluster chemistry, rare earth-amino acid cluster chemistry, and supramolecular inorganic assembly chemistry.*

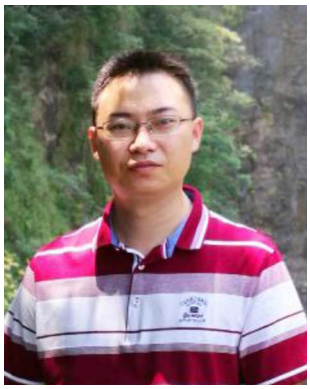

**Qi-Long Zhu**

*Qi-Long Zhu is a professor at Fujian Institute of Research on the Structure of Matter (FJIRSM), Chinese Academy of Sciences (CAS). He received his PhD degree in Physical Chemistry from FJIRSM-CAS in 2012. He then joined Prof. Qiang Xu's group at National Institute of Advanced Industrial Science and Technology (AIST, Japan) as a postdoctoral and JSPS (Japan Society for the Promotion of Science) fellow before taking his current faculty position in 2017. He has published more than 170 papers in refereed journals. His group currently focuses on heterogeneous catalysis and nonlinear optics.*


© 2024 The Author(s). Published by the Royal Society of Chemistry

Open Access Article. Published on 22 2024. Downloaded on 18/10/24 08:09:28.
This article is licensed under a Creative Commons Attribution 3.0 Unported Licence.

machine learning techniques such as SHG-weighted density analysis, the real-space atom-cutting technique, the dipole flexibility model, and partial response functionals.[28–38] Through a dual analysis involving both experimental and theoretical calculations, optical testing conditions can be determined for the identification of promising candidates as ideal IR-NLO materials.

To meet the demands of commercial applications, an ideal candidate for an IR-NLO crystal must fulfil several conditions.[39–53] Firstly, it should crystallize in a non-centrosymmetric (NCS) space group, which is a prerequisite for being a NLO crystal. Secondly, it should have a large $d_{eff}$ value, preferably more than 4 pm $V^{-1}$ (but even better if it exceeds 8 pm $V^{-1}$), in order to enhance the conversion efficiency. Additionally, it should have a high LIDT to withstand high power densities of fundamental frequency light waves. The LIDT is positively correlated with the band gap ($E_g$), which should be at least 3.0 eV, but it is even more desirable for it to be above 3.5 eV. Furthermore, the crystal should possess moderate birefringence ($\Delta n$) falling within the range of 0.03–0.10. Excessive birefringence can lead to the walk-off effect, while a small birefringence is not conducive to achieving phase-matching (PM). In addition, the crystal should have a wide optical transparency range that encompasses two significant atmospheric windows: 3–5 μm and 8–12 μm. Finally, the perfect IR-NLO crystal should exhibit stable physical and chemical properties, maintaining stability even when exposed to the air. It should also demonstrate thermal stability, which is advantageous for growing large-sized crystals. Among the various families of materials, chalcogenides show promising potential as excellent candidates for IR-NLO crystals. Extensive research has been conducted on these materials, demonstrating their ability to achieve a superior balance between $d_{eff}$ and $E_g$ compared to other families.

Rare-earth (RE)-based chalcogenides, which are a subset of chalcogenides, continue to garner attention from researchers due to the unique properties of lanthanide elements. According to Pearson's hard and soft acid–base theory,[54] $RE^{3+}$ cations are categorized as hard bases. As a result, the bonds formed between these cations and anions exhibit a certain degree of ionic character, similar to alkaline earth metal cations. Additionally, the covalent nature of these bonds is primarily derived from the outer 5d and 6s orbitals. The 4f orbitals situated in the inner shell receive shielding from the outer 5s and 5p electrons, limiting their contribution to bonding. As the atomic number increases, the 4f orbitals become more dispersed, causing these electrons to not fully occupy the inner regions of the 5s and 5p orbitals. This incomplete shielding effect on the nucleus results in the phenomenon known as lanthanide contraction. Consequently, the ionic radii of $Sc^{3+}$ and $Y^{3+}$ are similar to those of $Lu^{3+}$ and $Er^{3+}$ in the lanthanide series, hence, Y is classified as a member of the RE elements.

Due to the relatively large size of $RE^{3+}$ cations, they can accommodate higher coordination numbers. Their common coordination numbers are typically less than or equal to 9, approaching the sum of the 6s, 6p, and 5d orbitals, and can even reach up to 12. This complexity in coordination numbers contributes to the diverse geometric configurations of their polyhedra. The combination of the high coordination numbers and moderate positive charge of $RE^{3+}$ cations enables them to effectively disperse excess negative charges on anionic groups. This dispersion reduces the mutual attraction between anionic groups, presenting an opportunity to obtain low-dimensional anionic framework materials.

So far, numerous reviews on IR-NLO materials have been published. While there are a few examples involving a small amount of RE-based materials,[55–67] there has been no systematic overview analyzing and summarizing the fascinating RE-based chalcogenide family. In order to better illustrate the advantages of RE-based chalcogenide compounds and address the challenges in this field, this paper provides detailed explanations for 85 representative examples out of over 400 NCS compounds.[68–187] These examples are categorized into four groups based on the various asymmetric building motifs: (1) RE-based chalcogenides containing tetrahedral motifs; (2) RE-based chalcogenides containing lone-pair-electron motifs; (3) RE-based chalcogenides containing $[BS_3]$ and $[P_2Q_6]$ motifs; and (4) RE-based chalcohalides and oxychalcogenides. Finally, the conclusions and perspectives for RE-based chalcogenides and their derivatives are provided for further exploration.

## 2. RE-based chalcogenides containing various asymmetric building motifs

### 2.1. RE-based chalcogenides containing tetrahedral motifs

Spontaneous self-aggregation of a single $[MQ_4]$ anion disperses negative charges and increases the likelihood of acquiring a high-dimensional framework. RE cations exhibit excellent abilities to disperse negative charges, resulting in the formation of RE–Q bonds when charges are transferred to the anion. This creates favourable conditions for the generation of low-dimensional anionic frameworks. Additionally, the charge transfer optimizes the distribution of electrons in the compound, contributing more effectively to the NLO effects under the synergistic action of the polyhedral $[REQ_n]$ and tetrahedral $[MQ_4]$ asymmetric building motifs. In the $La_3LiM^{IV}S_7$ ($M^{IV}$ = Ge and Sn) system, the presence of a closed-ring structure for La–S–$M^{IV}$ reveals the existence of d–p π bonds attributed to the La-5d orbitals and S-3p orbitals. However, the empty 5d orbitals of $La^{3+}$ lack additional 5d electrons to form d–p back-bonding π bonds. As a result, the formation of extra bonds between $RE^{3+}$ and $Q^{2-}$ is hindered, limiting the enhancement of induced dipole moment oscillations. On the other hand, the lack of d electrons can be seen as an advantage as it avoids d–d and f–f transitions and enables better absorption of light. Next, the twelve systems containing tetrahedral motifs are introduced.

**2.1.1. $RE_3GaS_6$ (RE = Y, Dy, Ho, and Er).** The crystal structure of $RE_3GaS_6$ (RE = Dy, Y, Ho, and Er) was first reported in 1971 based on powder XRD data.[68] However, the linear and NLO properties of these compounds were not systematically studied and reported by Guo's group until 2013[69] and 2021,

Open Access Article. Published on 22 2024. Downloaded on 18/10/24 08:09:28.
This article is licensed under a Creative Commons Attribution 3.0 Unported Licence.

respectively.[70] High-quality single crystals of $RE_3GaS_6$ were obtained through solid-state reactions with KI as a flux. These chalcogenides are isomorphic and adopt the orthorhombic space group $Cmc2_1$. The structures consist of two types of functional primitives: [$RES_7$] monocapped trigonal prisms and [$GaS_4$] tetrahedra. The overall structure can be described as [$RES_7$] functional primitives constructing a 3D network, with Ga atoms occupying the tetrahedral cavities (see Fig. 1). Each tetrahedral cavity is formed by 10 [$RES_7$] units, with 3 sharing an S-edge and 7 sharing an S-corner with the Ga atom.

The results of the SHG test indicate that the [$RES_7$] functional primitives play a key role in the NLO activity, in addition to the [$GaS_4$] tetrahedron. The $d_{eff}$ of $RE_3GaS_6$ increases as the Shannon ionic radius of the $RE^{3+}$ ion decreases, namely, in the approximate sequence $Dy_3GaS_6 < Ho_3GaS_6 \approx Y_3GaS_6 < Er_3GaS_6$ when irradiated under a 2100 nm laser. This increase in $d_{eff}$ can be attributed to the increasing covalent bond feature of the RE–S bonds. Upon comparing the calculation results for $RE_3GaS_6$, it can be concluded that the frontier orbitals of all compounds are primarily influenced by the RE element and S, with very little involvement of Ga. Additionally, the calculated SHG coefficients for these sulfides closely match their experimental $d_{eff}$. Furthermore, the calculated value of $\Delta n$, which determines the phase-matchability of IR-NLO materials, is also in line with experimental PM behaviors.

**2.1.2. $Eu_8Sn_4Se_{20}$.** As a member of the $(M^{II}{}_2M^{IV}Q_5)_n$ family ($M^{II}$ = divalent metals, Eu, Yb, Pb, and Sn; $M^{IV}$ = group 14 metals; Q = S, Se, and Te; $n$ = 1, 2, and 4), $Eu_8Sn_4Se_{20}$ is the first material to demonstrate NLO activity, despite the presence of some NCS structures within this system. Although the synthesis, structure, and optical $E_g$ of $Eu_8Sn_4Se_{20}$ were reported by Dorhout and colleagues in 2001,[71] its NLO performance was not reported until 2020 by Guo's group.[72]

The structure of $Eu_8Sn_4Se_{20}$, which belongs to the orthorhombic space group $P2_12_12$, is displayed in Fig. 2a. The fundamental structural components consist of discrete [$Sn_4Se_{14}$] tetra-nuclear clusters and [$Se_3$] trimers. The

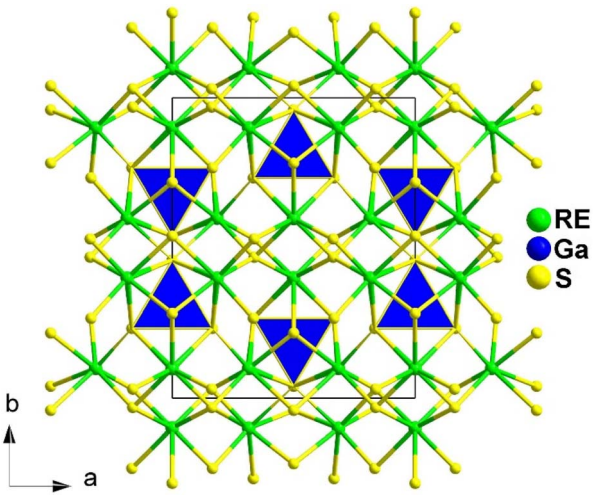


Fig. 1 Structures of $RE_3GaS_6$ along the $c$ axis with unit cell and discrete [$GaS_4$] polyhedra (blue) outlined.

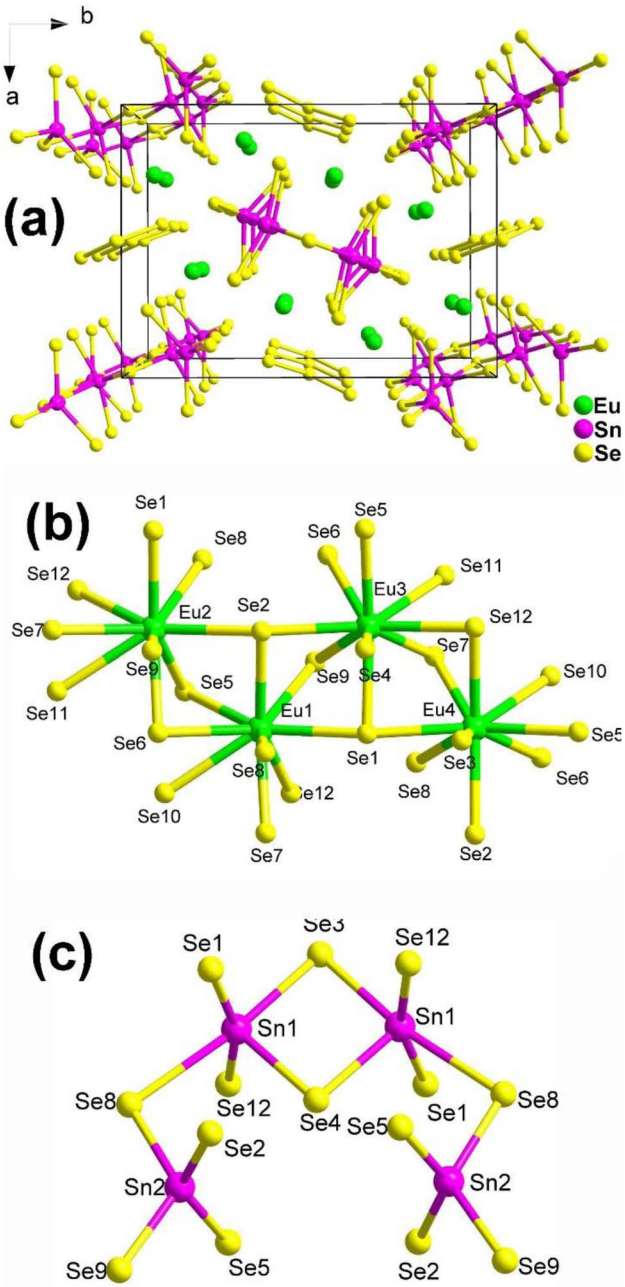


Fig. 2 (a) Central projection of $Eu_8Sn_4Se_{20}$ along the $c$ axis with the unit cell outlined; (b and c) coordination environment of the crystallographically independent Eu atoms and the discrete [$Sn_4Se_{14}$] tetra-nuclear cluster.

coordination environments of the Eu and Sn atoms in the structure are depicted in Fig. 2b and c. It is worth noting that Guo's group, through literature research and detailed structural analysis, pointed out in their report that the coordination geometry of Sn should be more reasonable for four-fold-coordination and six-fold-coordination, contrary to the 4- and 5-coordination mentioned in Yang's article.

Experimental results reveal that $Eu_8Sn_4Se_{20}$ possesses an indirect $E_g$ of 1.33 eV and displays antiferromagnetic-type behaviour. Most significantly, $Eu_8Sn_4Se_{20}$ exhibits SHG activity


© 2024 The Author(s). Published by the Royal Society of Chemistry

Open Access Article. Published on 22 2024. Downloaded on 18/10/24 08:09:28.
This article is licensed under a Creative Commons Attribution 3.0 Unported Licence.

($1 \times \alpha$-$SiO_2$ in the range of 150–210 μm under 2010 nm laser radiation), although the intensity is not particularly promising. Dipole moment measurements indicate that the majority of the dipole moment vectors of Eu/Se are in opposite directions, resulting in smaller dipole moments. This could be the primary reason for the compound's weak SHG signals.

**2.1.3. $EuCu_2M^{IV}Q_4$ ($M^{IV}$ = Si, Ge; Q = S, Se).** $EuCu_2GeS_4$ and $EuCu_2SnS_4$ were first synthesized in 2003 by Jaime Lanos.[73] Furthermore, in 2009, Jennifer A. Aitken obtained $EuCu_2SnS_4$ once again.[74] In 2019, Guo's group was able to obtain $EuCu_2GeS_4$ along with two new compounds, $EuCu_2GeSe_4$ and $EuCu_2SiS_4$, through a high-temperature solid-phase method.[75]

Although these compounds have the same composition ratio, they crystallize in three different spatial groups represented by the compounds $EuCu_2SiS_4$ (space group: $P3_121$), (b) $EuCu_2GeS_4$ (space group: $P3_221$), and (c) $EuCu_2SnS_4$ (space group: *Ama*2). Compounds $EuCu_2SiS_4$ and $EuCu_2GeS_4$ have similar coordination geometries and crystal structures (Fig. 3a and b), while $EuCu_2SnS_4$ has completely different ones (Fig. 3c). Similar phenomena are also common in the $M^{II}M^{I}{}_2M^{IV}Q_4$ family.[188–192] Therefore, the description of their structures will only focus on $EuCu_2SiS_4$ and $EuCu_2SnS_4$.

In $EuCu_2SiS_4$, there is 1 Eu, 1 Cu, 1 Si, and 2 S atoms in the crystallographically unique unit. This structure can be seen as a 3D network formed by $[EuS_8]$ bicapped trigonal prisms, with Cu and Si atoms occupying the tetrahedral cavities (Fig. 3a). Each $[EuS_8]$ motif links 8 neighboring $[EuS_8]$ motifs *via* sharing vertexes and interconnects with 2, 4, and 2 $[CuS_4]$ tetrahedra by sharing corners, edges, and faces, respectively.

For $EuCu_2SnS_4$, there is 1 Eu, 1 Cu, 1 Sn, and 3 S atoms in its crystallographically unique units. It also demonstrates a 3D framework made of $[EuS_8]$ motifs, with each $[EuS_8]$ motif connecting with 4 and 2 neighboring $[EuS_8]$ and $[CuS_4]$ groups by sharing corners and edges, respectively. It also links 6, 2, and 2 $[SnS_4]$ tetrahedra through sharing vertexes, edges, and faces, respectively (Fig. 3c).

Although $EuCu_2M^{IV}Q_4$ ($M^{IV}$ = Si, Ge; Q = S, Se) belong to the NCS space groups, no apparent SHG signals were detected under the two most commonly used wavelengths of 1064 nm and 2100 nm. This result is completely different from the previously reported isomorphic compounds of alkaline earth metal groups with strong SHG signals, and the underlying mechanism is currently unclear.

**2.1.4. $RE_3M_{1-x}M'Q_7$ (RE = Y, La–Nd, Sm–Tm, Yb; M and M′ = metals or metalloids; Q = S, Se).** The compounds $RE_3M_{1-x}M'Q_7$, which represent a large and well-known class of chalcogenides (>400 compounds), have been extensively studied due to their intriguing structural chemistry and technologically relevant physical properties.[76–131] From a chemical perspective, the $RE_3M_{1-x}M'Q_7$ series can be seen as derivatives of the classic parent structure of ternary $Ce_3Al_{0.67}S_7$,[193,194] achieved through a chemical co-substitution route. In this study, two examples are presented as structural prototypes within the $RE_3M_{1-x}M'Q_7$ family: the $La_3CuSiS_7$-type structure (Fig. 4a) and the $La_3FeGaS_7$-type structure (Fig. 4b). In these structures, the M and M′ cations are located at specific sites and are limited to certain types of cations. For example, M can be located with

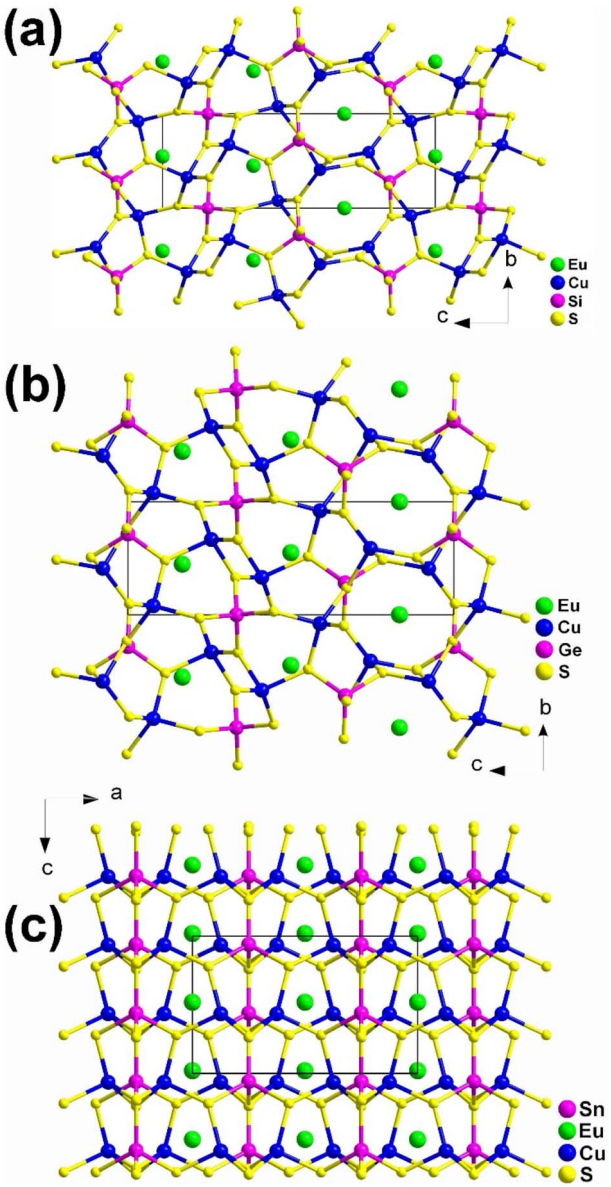


Fig. 3 Structures of (a) $EuCu_2SiS_4$ (space group: $P3_121$), (b) $EuCu_2GeS_4$ (space group: $P3_221$), and (c) $EuCu_2SnS_4$ (space group: *Ama*2) with the unit cell outlined.

different metal ions with various valence states, like monovalent IA and IB elements (with 100% occupancy), bivalent IIA, IIB, and transition-metal elements (with 50% occupancy), or occasionally trivalent IIIA elements (with sectional occupancy). M′, on the other hand, is typically associated with tetravalent IVA elements. The local coordination of M, situated at the 2a Wyckoff position, is either in a trigonal $[MQ_3]$ or an octahedral/trigonal antiprismatic $[MQ_6]$ configuration, while M′, located at the 2b Wyckoff position, exhibits a tetrahedral $[M'Q_4]$ coordination.

It is worth mentioning that the compounds in this family exhibit significantly different SHG intensities, the underlying reasons for which have not been revealed. In 2015, Chen's research group provided an unprecedented explanation for the

Open Access Article. Published on 22 2024. Downloaded on 18/10/24 08:09:28.
This article is licensed under a Creative Commons Attribution 3.0 Unported Licence.

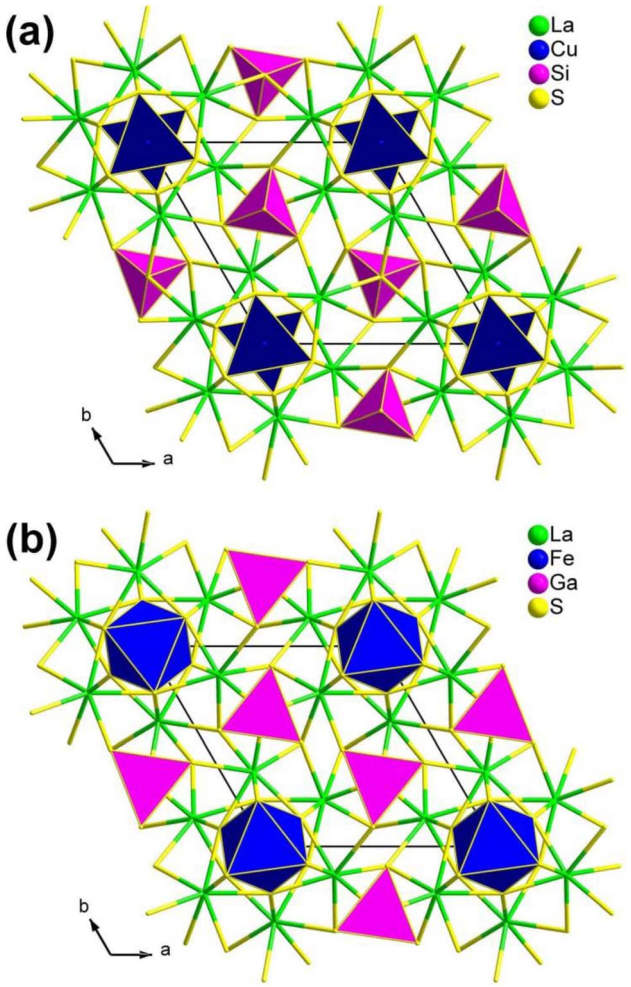


Fig. 4 Two classic structural types in the $RE_3M_{1-x}M^{IV}Q_7$ family: (a) $La_3CuSiS_7$-type and (b) $La_3FeGaS_7$-type structures with the unit cell outlined.

unique atomic distribution within this family, which is observed on both the octahedral 2*a* and tetrahedral 2*b* sites. This distribution is a direct consequence of the combined considerations of total energy and charge balance. What is even more intriguing is that, in the case of the $RE_3M_{1-x}M'Q_7$ family, the atomic distribution predominantly determines the NLO properties. Consequently, members exhibiting a high $d_{eff}$ value should adhere to the formula $RE_3M_{0.5}M^{IV}Q_7$.

Recently, Wu's group discovered a series of new isomorphic compounds, $RE_3LiMS_7$. Compared with the previously reported NPM behavior, these compounds exhibit useful PM features. Among them, $La_3LiGeS_7$ and $La_3LiSnS_7$ show strong $d_{eff}$ values (0.7 and 1.2 × $AgGaS_2$, respectively) and large LIDTs (6.0 and 2.5 × $AgGaS_2$, respectively). Detailed theoretical calculations indicate that the $d_{eff}$ values of the $RE_3LiMS_7$ family originate from the cooperation of intrinsic dipole moments and d–p delocalized-π-electron-induced dipole oscillations.

**2.1.5. $EuM^{II}M^{IV}Q_4$ ($M^{II}$ = Cd, Hg; $M^{IV}$ = Ge, Sn; Q = S, Se).** It is well known that tetrahedral $[MQ_4]$ functional primitives, such as $[M^{IV}Q_4]$ and $[M^{II}Q_4]$, make a large contribution to the SHG effect. Additionally, the introduction of two or more asymmetric building units helps in further modulating the crystal structure to obtain materials with SHG activities. Based on the reported $AEM^{II}M^{IV}Q_4$ compounds (AE = alkaline-earth metals; $M^{II}$ = transition metals; $M^{IV}$ = Si, Ge, and Sn, Q = S, Se), it is evident that this family is a promising candidate crystal for IR-NLO applications.[195–202] Considering that $Eu^{2+}$ and $AE^{2+}$ have similarities in their ionic radii and coordination configuration in metal chalcogenides, Kang's group successfully synthesized $EuCdGeQ_4$ in 2019, which was the first example containing a RE element in this family.[132] Subsequently, they introduced $Hg^{2+}$ with high polarizability to improve the $d_{eff}$ effect in the system, successfully obtaining two Hg-based compounds, $EuHgGeSe_4$ and $EuHgSnS_4$.[133]

$EuM^{II}M^{IV}Q_4$ ($M^{II}$ = Cd, Hg; $M^{IV}$ = Ge, Sn; Q = S, Se) are isostructural and crystallize in the NCS orthorhombic *Ama*2 space group. As shown in Fig. 5, a 2D covalent layer of $[M^{II}M^{IV}Q_4]^{2-}$ is made of tetrahedral $[M^{II}Q_4]$ and $[M^{IV}Q_4]$ motifs, and further stacks along the *a* direction with $[EuQ_8]$ units occupying the intervals. The geometry of the $[EuQ_8]$ units can be viewed as a distorted bicapped trigonal prism.

Owing to the structural traits that arrange the overall NLO-active motifs ($[M_{II}Q_4]$ and $[M^{IV}Q_4]$ units) in an orderly manner along a specific direction, all units exhibit strong $d_{eff}$ (approximately 2–4 × $AgGaS_2$@2090 nm) along with type-I PM behaviour. Furthermore, theoretical calculations and local dipole moment analyses suggest the significant contribution of distorted $[M^{II}Q_4]$ tetrahedra to the improved $d_{eff}$. These results confirm the intriguing potential applications of these materials as IR NLO crystals. This work also indicates the feasibility of replacing AE elements with RE elements in the exploration of novel IR-NLO candidates.

**2.1.6. $La_2Ga_2GeS_8$ and $Eu_2Ga_2GeS_7$.** Two new NCS quaternary chalcogenides, $La_2Ga_2GeS_8$ and $Eu_2Ga_2GeS_7$, were obtained through traditional solid-state reactions in 2011 by Chen's group.[134] $La_2Ga_2GeS_8$ belongs to the orthorhombic space

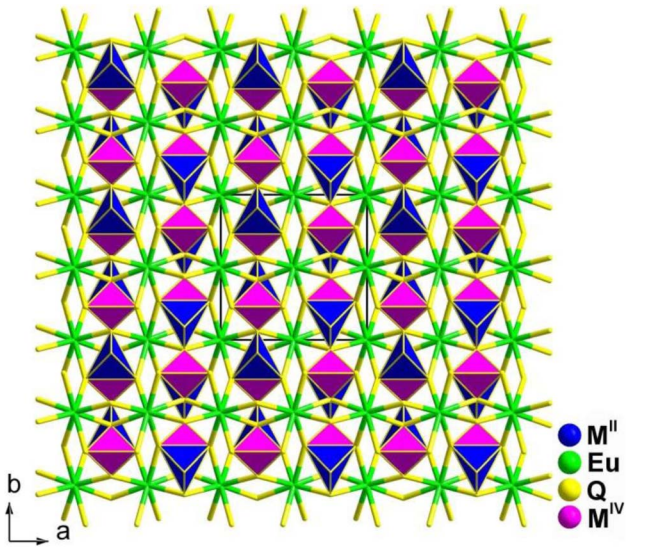


Fig. 5 Structures of $EuM^{II}M^{IV}Q_4$ (space group: *Ama*2) along the *c* axis with the unit cell outlined.


© 2024 The Author(s). Published by the Royal Society of Chemistry

Open Access Article. Published on 22 2024. Downloaded on 18/10/24 08:09:28.
This article is licensed under a Creative Commons Attribution 3.0 Unported Licence.

group $Cmc2_1$, while $Eu_2Ga_2GeS_7$ has a $Ca_2Ga_2GeO_7$-type structure in the tetragonal space group $P\bar{4}2_1m$. They formed stacked 2D layers of interconnected $[GaS_4]$ and $[GeS_4]$ tetrahedral functional primitives with $La^{3+}$ or $Eu^{2+}$ cations filled into these layers (Fig. 6). However, their functional primitives are linked in different fashions. The 2D $[Ga_2GeS_8]^{6-}$ layers in $La_2Ga_2GeS_8$ are formed by wavy 1D $[GaS_4]$ chains that are interlinked by individual $[GeS_4]$ units through sharing S corners. In contrast, the 2D $[Ga_2GeS_7]^{4-}$ layers in $Eu_2Ga_2GeS_7$ are formed by $[(GaS_4)_2]$ dimers connected *via* individual $[GeS_4]$ units.

It is worth mentioning that the number of terminal S atoms per formula plays a crucial role in determining the linkage of $[GaS_4]$ and $[GeS_4]$ functional primitives as well as the aggregation density of the anionic moieties. Theoretical analysis shows that RE cations narrow the $E_g$ but Li does not, and that all components affect the $d_{eff}$ through the electronic transitions from the S-3p state to the La/Eu/Li–S, Ga–S, and Ge–S antibonding states. This understanding may provide useful guidance for the further exploration and development of novel IR-NLO materials. Interestingly, the powder $Eu_2Ga_2GeS_7$ exhibits a large $d_{eff}$ (1.6 × $AgGaS_2$@2050 nm) with type-I NPM features, a wide transparent range, and a large theoretical $\Delta n$.

**2.1.7. $Ba_2REM^{III}Q_5$ (RE = Y, Ce, Nd, Sm, Gd, Dy, and Er; $M^{III}$ = Ga, In; Q = Se, Te).** Twenty chalcogenides with the formula $Ba_2REM^{III}Q_5$ were reported in 2012 and synthesized by Wu's group using a solid-state reaction.[135,136] They aimed to introduce f-block and p-block elements into chalcogenides to obtain unique structures and physical properties. In addition, AE metals were added to increase the $E_g$ of the chalcogenides.

According to the report, the $Ba_2REGaSe_5$ (RE = Y, Nd, Sm, Gd, Dy, and Er) and $Ba_2REGaTe_5$ (RE = Sm and Gd) compounds are isomorphic, with a centrosymmetric triclinic system in the $P\bar{1}$ space group. On the other hand, the $Ba_2REInSe_5$ (RE = Y, Nd, Sm, Gd, Dy, and Er), $Ba_2REGaTe_5$ (RE = Y, Dy, and Er), and $Ba_2REInTe_5$ (RE = Y, Ce, Nd, Sm, Gd, Dy, and Er) compounds belong to an NCS orthorhombic system in the $Cmc2_1$ space group. This discussion will focus solely on the NCS compounds.

Fig. 7 shows the structure of the NCS $Ba_2REM^{III}Q_5$ compounds. The structure consists of 1D $[REM^{III}Q_5]^{4-}$ chains formed by two types of chains connected through shared Q atoms. These two types of chains are constructed by $[REQ_6]$ octahedra and link together through shared edges, whereas $[M^{III}Q_4]$ tetrahedra connect through shared vertices.

Experimental results reveal that the $d_{eff}$ value of $Ba_2InYSe_5$ is similar to that of $AgGaSe_2$, making it the largest value among the compounds in this family. The $Ba_2REInSe_5$ (RE = Gd, Er) compounds exhibit very weak SHG responses, while the Nd, Sm, and Dy compounds show undetectable SHG responses. The detection of weak SHG signals or the failure to detect signals in the compounds of this system may be attributed to the absorption of fundamental and harmonic light by the sample. Similar phenomena have also been observed in other NCS

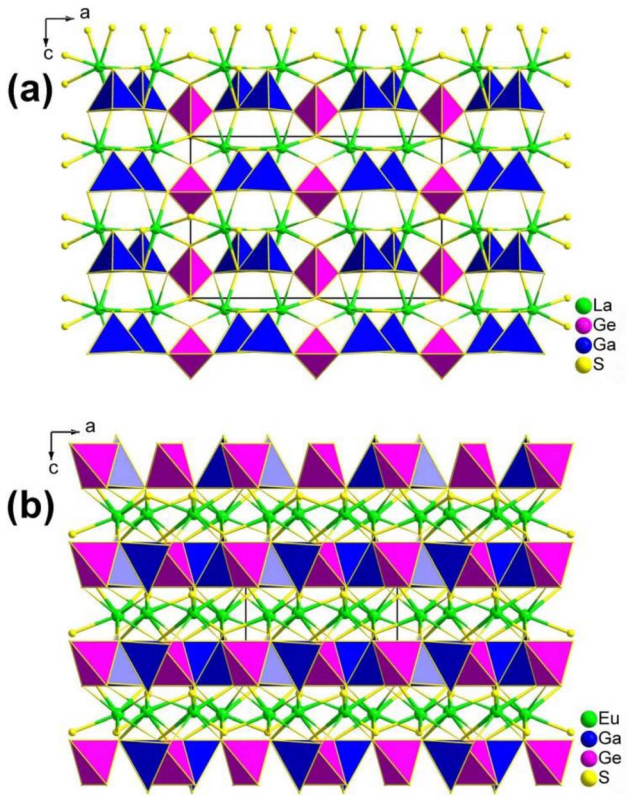


Fig. 6 Structures of (a) $La_2Ga_2GeS_8$ and (b) $Eu_2Ga_2GeS_7$ along the *ac* plane with the unit cell outlined.

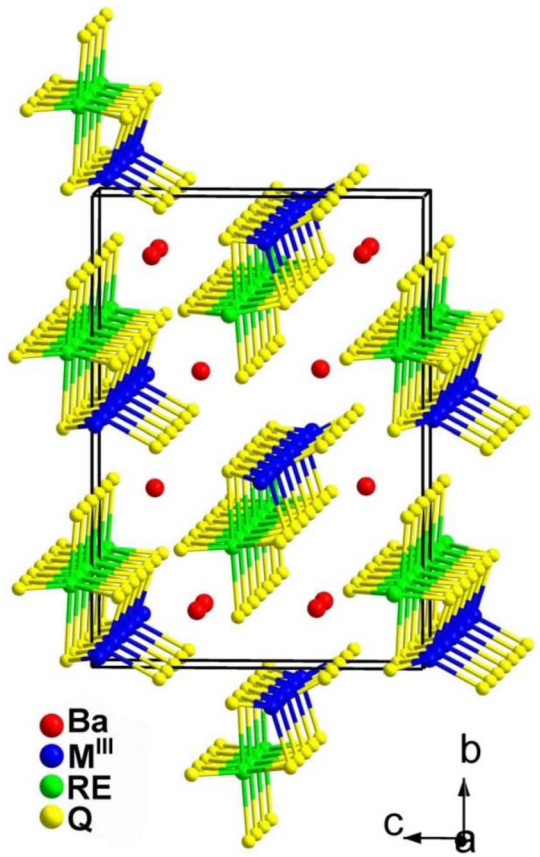


Fig. 7 Structure of $Ba_2REM^{III}Q_5$ along the *bc* plane with the unit cell outlined.

Open Access Article. Published on 22 2024. Downloaded on 18/10/24 08:09:28.
This article is licensed under a Creative Commons Attribution 3.0 Unported Licence.

chalcogenides.[203–205] On the other hand, it is evident that in the $Ba_2REInSe_5$ compounds, the RE metal cation does not impact the crystal structure but does affect the intensity of the $d_{eff}$.

**2.1.8. $Ba_4RE_2Cd_3S_{10}$ (RE = Sm, Gd, and Tb).** $Ba_4RE_2Cd_3S_{10}$ (RE = Sm, Gd, and Tb) is the only type of AE/RE/TM/Q (AE = alkaline earth elements; RE = rare-earth elements; M = main group elements; TM = d-block transition elements; and Q = chalcogen) system with an NCS space group. Previous reports on this system mainly focused on its magnetism.[206] However, in 2022, Zhu's research group conducted a systematic investigation of its linear and NLO properties for the first time.[137]

The preparation of the flat needle transparent-brown crystals of $Ba_4RE_2Cd_3S_{10}$ involved a solid-phase method of elemental mixtures in a $KCl/BaCl_2$ (1 : 3) flux at 1173 K. All of them are isostructural and adopt the NCS orthorhombic space group $Cmc2_1$ (no. 36). Fig. 8 displays a view of the structure of $Ba_4RE_2Cd_3S_{10}$ on the *bc* plane, where the most prominent feature is the 2D complex anionic $[RE_2Cd_3S_{10}]^{8-}$ layers stacked in an *ABABAB* fashion along the *ab*-plane, with discrete $Ba^{2+}$ cations located in between.

Remarkably, $Ba_4Sm_2Cd_3S_{10}$ exhibits a strong $d_{eff}$ (1.8 × $AgGaS_2$) and a significantly higher LIDT (14.3 × $AgGaS_2$). This is the first case of a quaternary AE/RE/TM/Q system possessing an IR-NLO property. Furthermore, the theoretical results for the structure–activity relationships suggest that the combined action of different types of NLO-active motifs (*i.e.*, $[RES_6]$ and $[CdS_4]$) contributes to the SHG activity.

**2.1.9. $LaAEM^{III}{}_3S_7$ (AE = Sr, Ca; $M^{III}$ = Al, Ga).** $LaCaGa_3S_7$ was first synthesized in 1987, and only its structure was reported at that time.[138] In 2022, Zhang's team synthesized $LaAEGa_3S_7$ (AE = Ca, Sr) again in a study that compared their specific properties and revealed a series of changes in analogues involving oxides, sulfides, and oxysulfides.[139] Subsequently, they obtained two other isomorphic $LaAEAl_3S_7$ (AE = Ca, Sr) compounds through homologous substitution.[140]

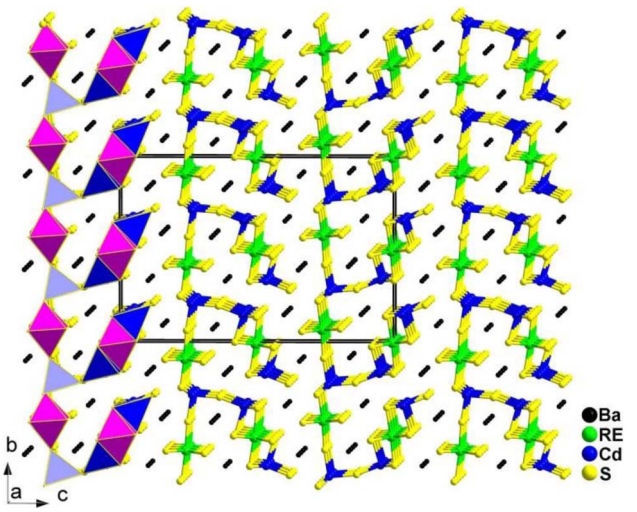


Fig. 8 Structure of $Ba_4RE_2Cd_3S_{10}$ along the *a* axis with the unit cell outlined.

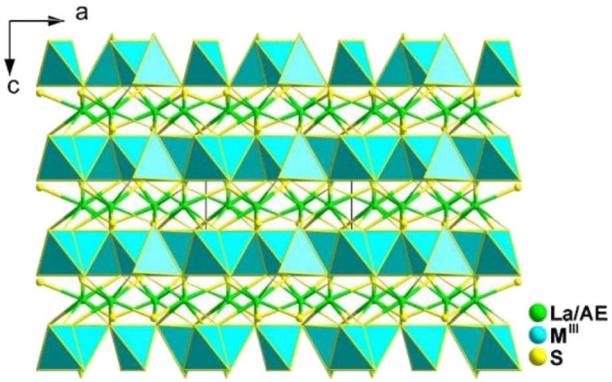


Fig. 9 Structure of $LaAEM^{III}{}_3S_7$ along the *b* axis with the unit cell outlined.

$LaAEM^{III}{}_3S_7$ adopt the $P\bar{4}2_1m$ space group of the tetragonal system. In the structure, La and AE atoms co-occupy the same position with occupation ratios of 50% and 50%. As shown in Fig. 9, one $[M^{III}S_4]$ motif is connected with four other $[M^{III}S_4]$ motifs to generate a $[M^{III}{}_5S_{16}]^{17-}$ windmill cluster and further interlink together to form a 2D Cairo pentagonal layer along the *c* direction. Polyhedral $[(La/AE)S_8]$ groups filled in the interlayers to bridge neighbouring layers together to build the overall 3D framework.

It should be noted that the 2D Cairo pentagonal layer in $LaAEAl_3S_7$ contributes to their excellent optical performance. This includes a large $d_{eff}$ (0.8–1.1 times that of $AgGaS_2$), a broad optical $E_g$ of 3.76–3.78 eV (the first known cases to achieve the breakthrough of the "3.5 eV wall" among all RE-based IR-NLO chalcogenides), high LIDTs (approximately 9 times that of $AgGaS_2$), and moderate $\Delta n$ (0.059 for the Ca-compound and 0.077 for the Sr compound at 2000 nm) for PM. These findings offer a new structural guidance route for the development of high-performance IR-NLO chalcogenides.

**2.1.10. $RE_2AE_3M^{IV}{}_3S_{12}$ (RE = La, Pr, Nd, Sm, Gd, Ho, and Er; AE = Sr, Ca; $M^{IV}$ = Si, Ge, and Sn).** Currently, a significant challenge in the field of IR-NLO is how to effectively combine and select asymmetric functional primitives to achieve NCS structures and strong $d_{eff}$. In 2023, Wu and co-workers achieved successful synthesis of 29 compounds by combining flexible $[SnS_n]$ ($n$ = 5 and 6) functional primitives with highly positively charge-balanced ions, such as $RE^{3+}$ and $AE^{2+}$ cations. These compounds included 12 NCS thiostannates, $RE_2Sr_3SnS_{12}$ (space group: $Pmc2_1$), and $RE_2Ca_3Sn_3S_{12}$ (space group: $P\bar{6}2m$), as well as 17 CS compounds, $RE_2AE_3Ge_3S_{12}$ and $RE_2AE_3Si_3S_{12}$, constructed from rigid $[GeS_4]$ or $[SiS_4]$ tetrahedra.[141,142]

$La_2Sr_3M^{IV}{}_3S_{12}$ ($M^{IV}$ = Si, Ge), $La_2Ca_3Sn_3S_{12}$, and $La_2Sr_3Sn_3S_{12}$ serve as three typical examples to illustrate the inherent structural features of the family (Fig. 10). The structure of $La_2Sr_3M^{IV}{}_3S_{12}$ ($M^{IV}$ = Si, Ge) exhibits isolated $[M^{IV}S_4]$ groups, and all the isolated $[M^{IV}S_4]$ groups located in the *c* direction are symmetrical. Additionally, the $[LaS_8]$ polyhedra are connected together to generate a 3D framework, while the polyhedral $[SrS_7]$ and $[SrS_9]$ groups are interconnected to create an isolated triple-chain structure. In the $La_2Ca_3Sn_3S_{12}$ structure, La and Ca atoms occupy the same


© 2024 The Author(s). Published by the Royal Society of Chemistry

Open Access Article. Published on 22 2024. Downloaded on 18/10/24 08:09:28.
This article is licensed under a Creative Commons Attribution 3.0 Unported Licence.

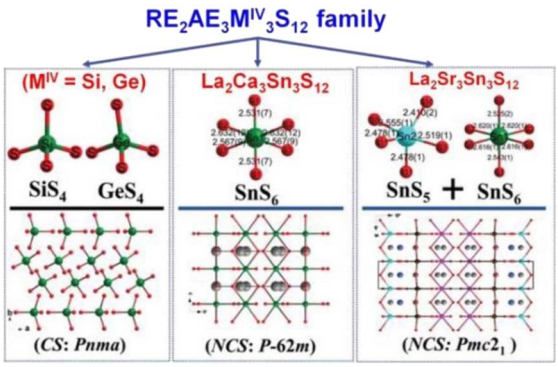


Fig. 10 CS-to-NCS structural transformation with varying anionic motifs in the $RE_2AE_3M^{IV}{}_3S_{12}$ family. This figure has been adapted from ref. 142 with permission from Wiley-VCH, copyright 2024.

positions and Sn atoms are coordinated to 6 S atoms to build the $[SnS_6]$ octahedron. The $[SnS_6]$ units interconnect with each other to form edge-sharing 1D $[(SnS_4)]_n$ chains, which are situated within the tunnels encircled by the polyhedral $[(La/Ca)S_7]$ and $[(La/Ca)S_9]$ motifs. It is worth noting that $[Sn^{IV}S_5]$ and $[Sn^{IV}S_6]$ units were only found in the structures of $La_2Sr_3Sn_3S_{12}$. The $[SnS_5]$ and $[SnS_6]$ units have no connection, and each forms isolated 1D chains with various linking modes. For instance, $[SnS_5]$ units are interlinked together *via* sharing vertexes to build 1D $[(SnS_4)]_n$ chains, while $[SnS_6]$ units interconnect with each other to generate edge-sharing 1D $[(SnS_4)]_n$ chains. The arrangement orientation of $[SnS_5]$ units in the unit cell demonstrates a nearly uniform arrangement along the *ab* plane.

The remarkable CS-to-NCS structural transition (from *Pnma* to $P\bar{6}2m$ to $Pmc2_1$) observed in the $RE_2AE_3M^{IV}{}_3S_{12}$ family indicates that the substitution of tetrahedral $[GeS_4]/[SiS_4]$ motifs with $[SnS_n]$ disrupts the original symmetry, resulting in the formation of the necessary NCS structures.

Significantly, the $[SnS_5]$ unit exhibits strong polarization anisotropy and hyperpolarizability, leading to significant performance improvements in NPM $d_{eff}$ for compounds like $La_2Ca_3Sn_3S_{12}$ (1.4 × $AgGaS_2$ and $\Delta n = 0.008$), compared to the strong PM $d_{eff}$ observed in compounds like $La_2Sr_3Sn_3S_{12}$ (3.0 × $AgGaS_2$ and $\Delta n = 0.086$). These findings demonstrate $[SnS_5]$ to be a promising "NLO-active motif".

By incorporating flexible $[SnS_n]$ ($n$ = 5 and 6) NLO-active motifs into the crystal structure, this study offers a viable approach for designing novel NCS thiostannates that exhibit very large SHG effects and significant optical anisotropy.

**2.1.11. $AREM^{IV}Q_4$ (A = Li, K, Rb, and Cs; RE = Y, La–Nd, Sm–Yb; $M^{IV}$ = Si, Ge; Q = S, Se).** Systematic exploratory efforts have resulted in the discovery of 46 new chalcogenides in this system. These include the $LiRESiS_4$ (RE = La, Ce), $KREM^{IV}Q_4$ (RE = Y, La–Nd, Eu–Tb; $M^{IV}$ = Si, Ge; Q = S, Se), and $AREM^{IV}Q_4$ (RE = La–Nd, Eu–Yb; $M^{IV}$ = Si, Ge; Q = S, Se).[143–148] Although they share the same 1 : 1 : 1 : 4 stoichiometry, these compounds belong to different crystal systems and exhibit different structural symmetries.

Two new RE-based thiosilicates, specifically, $RELiSiS_4$ (Ln = La and Ce), were successfully discovered by aliovalent substitution based on $SrCdSiS_4$ as a parent compound in 2023 by Mao's group. They were synthesized using $Li_2S$, $RE_2S_3$, $SiS_2$, and S in a molar ratio of 3 : 1 : 3 : 8 through a high-temperature solid-state method at 1073 K. They are isostructural and belong to the orthorhombic space group *Ama*2 (no. 40). As shown in Fig. 11a, a 2D covalent layer of $[LiSiS_4]^{3-}$ is constructed by tetrahedral $[LiS_4]$ and $[SiS_4]$ motifs, which further stacks along the *a* direction with $[RES_8]$ units occupying the intervals. Interestingly, this is the first observation of this linking mode in the Li–Si–S system. $RELiSiS_4$ (RE = La and Ce) also exhibit

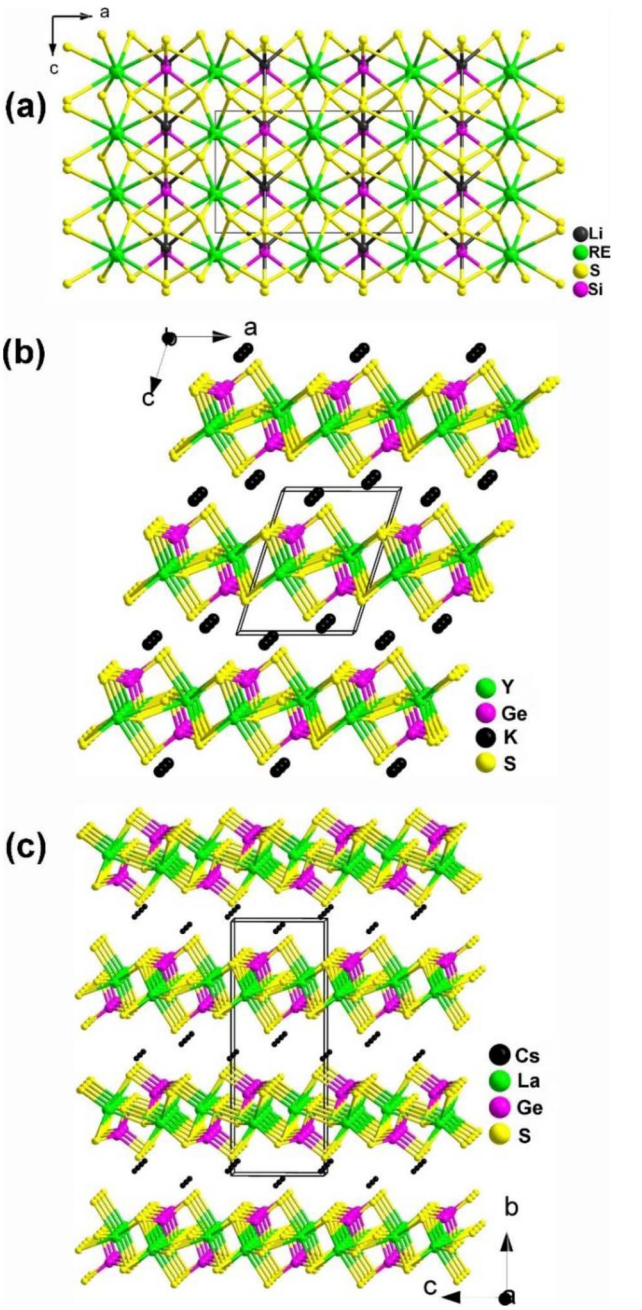


Fig. 11 Structures of (a) $LiRESiS_4$ (space group: *Ama*2), (b) $KYGeS_4$ (space group: $P2_1$), and (c) $CsLaGeS_4$ (space group: $P2_12_12_1$) with the unit cell outlined.

Open Access Article. Published on 22 2024. Downloaded on 18/10/24 08:09:28.
This article is licensed under a Creative Commons Attribution 3.0 Unported Licence.

perfectly balanced properties for IR-NLO chalcogenides: the largest $d_{eff}$ among all reported thiosilicates (2.0 and 2.1 × $AgGaS_2$@2050 nm for $LaLiSiS_4$ and $CeLiSiS_4$, respectively) with PM ability, high LIDTs (14 and 9 × $AgGaS_2$@1064 nm), large $E_g$ (3.71 and 2.92 eV), wide IR transmission window (0.35–18 μm), and good thermal stability above 973 K. This study not only enriches the structural chemistry of RE-based thiosilicates, but also offers an efficient method to design novel high-performance IR-NLO candidates.

$KREM^{IV}Q_4$ compounds (RE = Y, La–Nd, Eu–Tb; $M^{IV}$ = Si, Ge; Q = S, Se) belong to the NCS monoclinic space group $P2_1$ (no. 4) and are isostructural. Therefore, for the purposes of this description, only the structure of $KYGeS_4$ will be detailed as a representative. This compound was successfully synthesized in 2021 by Mei's group using a charge transfer engineering strategy. Fig. 11b shows that the $[YS_7]$ and $[GeS_4]$ motifs are interconnected by sharing polyhedral edges, and the $[YS_7]$ units are linked to one another through sharing vertexes to generate the infinite 2D $[YGeS_4]_n$ layers. The interlayer interstices are filled by $K^+$ cations to maintain charge balance. It is noteworthy that both $[GeS_4]$ and $[YS_7]$ polyhedra are uniformly arranged along the *ab* plane, which facilitates the positive superposition of microscopic second-order susceptibility, resulting in a strong $d_{eff}$. $KYGeS_4$ overcomes the $E_g$ limitation found in rare earth chalcogenides with the largest $E_g$ (3.15 eV) within this material system, while displaying a significant $d_{eff}$ (*ca.* 1.0 × $AgGaS_2$). Moreover, $KYGeS_4$ is the first RE-based chalcogenide to surpass the "3.0 eV wall" observed in IR-NLO crystals.

Isostructural $AREM^{IV}Q_4$ compounds (RE = La–Nd, Eu–Yb; $M^{IV}$ = Si, Ge; Q = S, Se) were synthesized by Loye and co-workers using a molten alkali halide flux growth method in 2019. All of them adopt the NCS monoclinic space group $P2_12_12_1$ (no. 19), and in this discussion, we will focus on the structure of $CsLaGeS_4$ as an example. $CsLaGeS_4$ can be easily obtained by adding Ge to the reaction mixture of $La_2S_3$ and S in the CsCl/KCl eutectic flux. In the structure of $CsLaGeS_4$, there are $[LaS_7]$ monocapped trigonal prisms and $[GeS_4]$ tetrahedrons. These polyhedral $[LaS_7]$ motifs and tetrahedral $[GeS_4]$ units interlink together through the sharing edge to generate the infinite 2D $[LaGeS_4]^-$ slabs in the *ac* plane. The $Cs^+$ cations fill in the gaps between the layers and act as charge balancers. Unfortunately, only $CsLaGeS_4$ was found to be SHG-active, exhibiting nearly half the intensity of $\alpha$-$SiO_2$ when irradiated with a Nd:YAG 1064 nm laser. This compound also behaves as a semiconductor with an $E_g$ of 3.60 eV based upon UV-vis diffuse reflectance measurements.

**2.1.12. $K_3REP_2S_8$ (RE = Y, Ho, and Er).** In 2023, a new series of RE-based thiophosphates, $K_3REP_2S_8$, was successfully prepared and systematically investigated by Wu and co-workers.[149] Microcrystals of $K_3REP_2S_8$ were obtained with the stoichiometric K, $RE_2S_3$, P, and S by spontaneous crystallization. Single-crystal XRD structural refinement indicates that $K_3REP_2S_8$ adopts two different types of space groups: NCS $P2_1$ (RE = Y, Ho, and Er) and CS $P2_1/c$ (RE = Pr, Sm, and Gd). The similarities and differences in their structures are as follows: (i) they possess the same asymmetric motifs consisting of 3 K, 1 RE, 2 P, and 8 S sites but different *Z* values (*Z* = 2 for NCS; *Z* = 4 for CS) in a unit cell; (ii) $[RES_8]$ dodecahedra connect each other *via* sharing vertexes to generate the 1D isolated $[RES_7]_n$ chains (Fig. 12a) in NCS structure, which is different than the 1D $[RES_6]_n$ chain formed by edge-sharing $[RES_8]$ units in the CS structure; (iii) isolated $[PS_4]$ motifs link with $[RES_8]$ units to produce the 1D $[REP_2S_8]^{3-}$ chains through sharing faces, edges, and vertexes in the NCS structure, which is distinguished from the interconnections (only edge-sharing) between the $[RES_8]$ and $[PS_4]$ motifs in the CS structure. In addition, the inherent connection mode between the $[RES_8]$ and $[PS_4]$ motifs in the K–RE–$P^V$–S system was investigated (Fig. 12b) to evaluate the relationships between local asymmetry and the centrality of the overall network. The survey results indicate that most of them belong to the CS space group, and due to local symmetry, have edge sharing patterns between $[RES_8]$ and $[PS_4]$ motifs. That is, the CS-to-NCS structural transformation in the $K_3REP_2S_8$ family can be attributed to the RE cation-size effect.

Remarkably, NCS $K_3REP_2S_8$ displaying strong PM $d_{eff}$ (1.1–1.4 × $AgGaS_2$) and large optical anisotropy ($\Delta n$ = 0.084–0.099) were also proven to be promising IR-NLO candidates. The SHG density and dipole moment calculations indicate that the synergistic effect between the $[RES_8]$ and $[PS_4]$ units creates an inherent NLO origin, which verifies that RE-based thiophosphates can be regarded as an excellent research system for exploring novel IR-NLO chalcogenides.

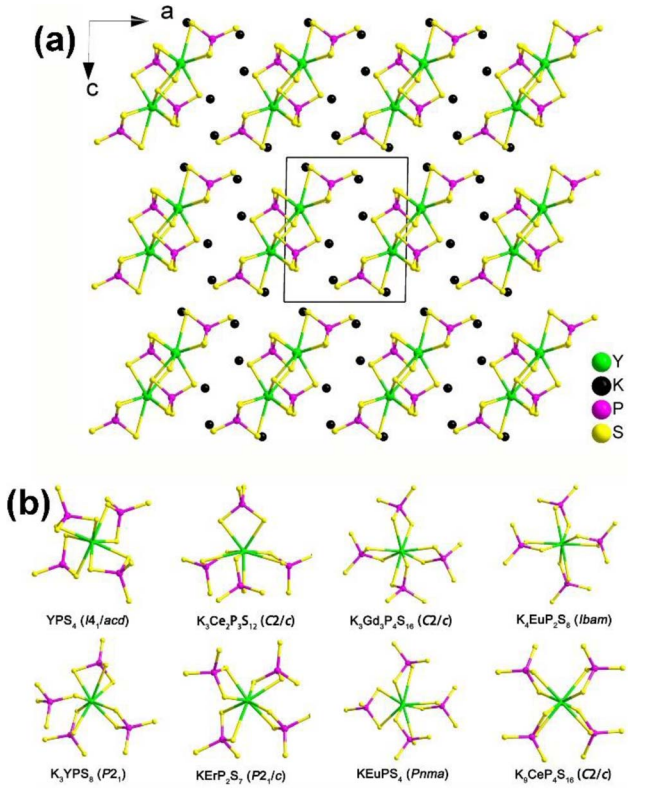


Fig. 12 (a) Structure of $K_3YP_2S_8$ along the *ac* plane with the unit cell outlined and (b) comparison on the local coordination modes between $[RES_8]$ and $[PS_4]$ motifs in the reported K/RE/P(V)/S family.


© 2024 The Author(s). Published by the Royal Society of Chemistry

Open Access Article. Published on 22 2024. Downloaded on 18/10/24 08:09:28.
This article is licensed under a Creative Commons Attribution 3.0 Unported Licence.

### 2.2. RE-based chalcogenides containing lone-pair-electron motifs

The unique structural characteristics of polyhedra formed by cations that contain a stereochemically active lone pair (SCALP) give rise to a strong local built-in electric field, resulting in a significant dipole moment. As a result, neighbouring polyhedra with a SCALP often connect in opposite orientations, increasing the likelihood of crystallizing in an NCS space group.[207–214] The inclusion of highly positively charged RE cations effectively creates a built-in electric field within their immediate surroundings. This takes advantage of the electrostatic interaction between the SCALP electrons and the RE cations to align the initially different orientations, thereby facilitating the macroscopic overlap of the static dipole moments. This alignment enhances the chances of crystallization in an NCS space group. Three types of RE-based chalcogenides containing lone-pair-electron motifs are presented below: $RE_8Sb_2S_{15}$ (RE = La, Ce, Pr, and Nd), $La_2CuSbS_5$, and $RE_4M^{III}SbQ_9$ (RE = Y, La, Pr, Nd, Sm, Tb, Dy, and Ho; $M^{III}$ = Ga, In; Q = S, Se).

**2.2.1. RE $_8Sb_2S_{15}$ (RE = La, Ce, Pr, and Nd).** Through the combination of Sb with stereochemically active lone-pair electrons and RE with high coordination numbers (CN), Zhao and co-workers successfully synthesized $RE_8Sb_2S_{15}$ (RE = La, Pr, and Nd) in 2015.[150] However, $Nd_8Sb_2S_{15}$ could not be obtained as a single phase.[151] Although $Pr_8Sb_2S_{15}$ had previously been obtained in 1981, its SHG performance was not reported.[152] In 2017, Zhao obtained $Ce_8Sb_2S_{15}$ *via* high-temperature solid-state synthesis.[153] The lanthanide contraction from La to Nd does not affect the crystal structure of these compounds, as they are isostructural and adopt the NCS tetragonal $I4_1cd$ space group. The structure of $RE_8Sb_2S_{15}$ with the unit cell outlined is shown in Fig. 13a. The structure consists of discrete $[SbS_3]^{3-}$ trigonal pyramids arranged approximately along the [001] direction, filled by $RE^{3+}$ cations and $S^{2-}$ anions. $RE_1$ and $RE_2$ have normal monocapped trigonal prismatic coordination environments, whereas the other two crystallographically unique RE positions, RE3 and RE4, are occupied in approximately square antiprismatic modes (Fig. 13b). Therefore, the formula of $RE_8Sb_2S_{15}$ can be written as $[(RE^{3+})_8([SbS_3]^{3-})_2(S^{2-})_9]$.

The compound $La_8Sb_2S_{15}$ shows an $E_g$ of 2.30 eV and a high effective $d_{eff}$ of 1.2 × $AgGaS_2$ (at 74–106 μm under 2050 nm laser irradiation) with NPM behavior. However, no significant $d_{eff}$ was observed for $Pr_8Sb_2S_{15}$, which may be linked to its poor crystallinity.

**2.2.2. $La_2CuSbS_5$.** A millimeter-grade single crystal of $La_2CuSbS_5$ was first prepared by Zhu's group in 2019 using a $BaCl_2$/CsBr flux at a temperature of 1273 K.[154] Although this compound was discovered in 2016, no properties were reported at that time due to the inability to obtain a pure phase.[155]

Single-crystal XRD result indicated that $La_2CuSbS_5$ belongs to the NCS orthorhombic system with the space group *Ima*2 (no. 46). The structure of $La_2CuSbS_5$ made of several distinct units, namely, $[LaS_{10}]$ polyhedra, $[CuS_4]$ tetrahedra, and $[SbS_4]$ pyramids. Fig. 14a depicts the projection of $La_2CuSbS_5$ viewed down the *ab* plane. The 3D network is constructed from two types of 2D layers (La/Cu/S and La/Sb/S) that are interconnected through

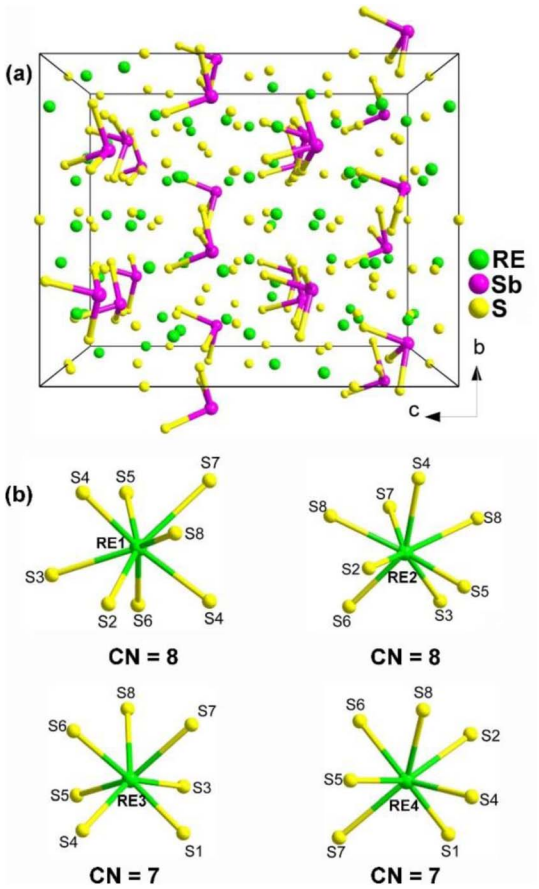


Fig. 13 (a) Central projection of $RE_8Sb_2S_{15}$ with the unit cell outlined and (b) coordination environment of crystallographically independent RE atoms.

shared S–S apexes and edges. The detailed coordination environment of the La atoms is shown in Fig. 14b.

Moreover, $La_2CuSbS_5$ can be seen as a result of the stereochemically active lone pair induction (SCALPI) strategy, which is based on the previously known CS $La_2CuInS_5$. Investigation into its optical properties showed that $La_2CuSbS_5$ displays a suitable PM $d_{eff}$ (0.5 × $AgGaS_2$) and a large LIDT (6.7 × $AgGaS_2$), making it a promising candidate for IR-NLO materials. Furthermore, theoretical calculations support the notion that the $d_{eff}$ can be attributed to the synergistic effects of the functional primitives, with a particular emphasis on the $[SbS_4]$ motifs. These results confirm the practicality of utilizing the SCALPI strategy for the design and exploration of new IR NLO crystals.

**2.2.3. $RE_4M^{III}SbQ_9$ (RE = Y, La, Pr, Nd, Sm, Tb, Dy, and Ho; $M^{III}$ = Ga, In; Q = S, Se).** Single-crystal XRD structural refinement indicates that $RE_4M^{III}SbQ_9$ adopts two different types of crystal structures: $RE_4GaSbS_9$ (RE = Pr, Nd, Sm, Gd to Ho and Y) and $RE_4InSbQ_9$ (RE = La to Nd, Sm, Y; Q = S, Se).[156–162] As shown in Fig. 15, the structures of these compounds have both similarities and differences. Firstly, the isostructural Ga-analogues belong to the orthogonal system [space group: *Aba*2 (no. 41)], while the isostructural In-analogues crystallize in the tetragonal system [space group: $P4_12_12$ (no. 92) or $P4_32_12$ (no. 96)]. Secondly, they have similar asymmetric motifs consisting of 4

Open Access Article. Published on 22 2024. Downloaded on 18/10/24 08:09:28.
This article is licensed under a Creative Commons Attribution 3.0 Unported Licence.

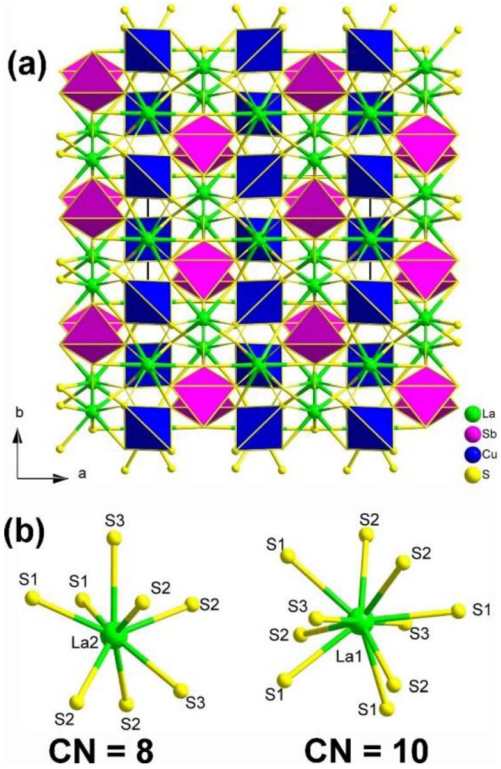


Fig. 14 (a) Structure of $La_2CuSbS_5$ along the *ab* plane with the unit cell outlined; (b) coordination environment of crystallographically independent La atoms.

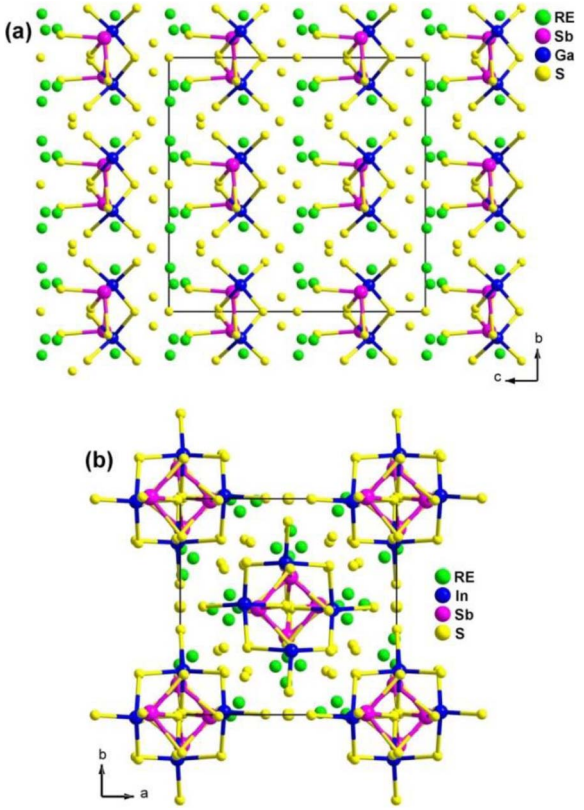


Fig. 15 Structures of (a) $RE_4GaSbS_9$ and (b) $RE_4InSbS_9$ with the unit cell outlined.

RE, 1 $M^{III}$, 1 Sb, and 9 Q sites, as well as the same $Z$ values in a unit cell. Lastly, in the $RE_4GaSbS_9$ compounds, the $[Ga_2S_6]$ and $[Sb_2S_5]$ functional primitives are arranged around a 2-fold screw axis, with neighboring dimers oriented in the same direction (Fig. 15a). In contrast, in the $RE_4GaSbQ_9$ compounds, the $[In_2Q_6]$ and $[Sb_2Q_5]$ functional primitives are arranged in the opposite direction (Fig. 15b).

The experimental results demonstrate that $RE_4GaSbS_9$ and $RE_4InSbQ_9$ exhibit different NLO performances. The former is NPM while the latter is PM under the same test conditions. For example, among the Ga analogues, $Sm_4GaSbS_9$ shows the strongest $d_{eff}$ (3.8 × $AgGaS_2$ in the particle size of 46–74 μm) with NPM features at 2050 nm. Among the In analogues, $La_4InSbS_9$ exhibits a strong $d_{eff}$ (1.5 × $AgGaS_2$ in the particle size of 150–210 μm) with PM features at 2050 nm.

The theoretical results suggest that the SHG response of $RE_4GaSbS_9$ can be attributed to the electronic transitions from the S-3p states in the valence bands to the Sb–S and RE–S antibonding states. On the other hand, the SHG response of $RE_4InSbQ_9$ is attributed to the thermal vibrations of the lattice.

### 2.3. RE-based chalcogenides containing $[BS_3]$ and $[P_2Q_6]$ motifs

The $[BS_3]$ motif, with its distinctive planar conjugated $\pi_4^6$ electron structure, is a crucial functional unit. Its introduction not only benefits the synergistic enhancement of NLO response and LIDT, but also has a significant impact on birefringence. By anchoring RE cations to the $[BS_3]$ unit, the arrangement of the $[BS_3]$ unit is optimized. The bonding interaction between them synergistically enhances the contribution to conductive bands, reinforcing the contribution to the empty virtual–hole transition process by the low-lying 4f or 5d orbitals in the rare earth ions and the π* anti-bonding orbitals of the $[BS_3]$ unit. For the crossed ethane configuration of the $[P_2Q_6]$ unit, the 6 exposed Q atoms serve as sites to balance its negative charge through chemical bonding. The high coordination number of rare earth ions precisely matches this unit, allowing one RE cation to bond with one or even multiple $[P_2Q_6]$ units. This maximizes the functionality of this basic unit and synergistically enhances the NLO effects in conjunction with $[REQ_n]$ polyhedra. In the following discussion, four systems are introduced: $REBS_3$ (RE = La, Ce, Pr, Nd, Sm, and Tb), $Ca_2RE(BS_3)(SiS_4)$ (RE = La, Ce, and Gd), $Eu_2P_2S_6$, and $KREP_2Se_6$ (RE = Sm, Tb, and Gd).

**2.3.1. $REBS_3$ (RE = La, Ce, Pr, Nd, Sm, and Tb).** A new class of NLO materials known as thioborates potentially possesses high LIDTs, diverse structures, large $d_{eff}$ values, and wide optical transmittance. Among them, $REBS_3$ (RE = La, Ce, Pr, Nd, Sm, and Tb) were first to be reported by Hunger *et al.* in 2010, but they required rigorous experimental conditions of high temperature and pressure.[163–166] Moreover, the samples produced using this method were only polycrystalline powders. Therefore, researchers like Hans-Conrad zur Loye *et al.* explored a new method using the boron–chalcogen mixture approach, with raw materials including $RE_2O_3/CeO_2$, B, S, and $K_2S$/NaI–CsI


© 2024 The Author(s). Published by the Royal Society of Chemistry

Open Access Article. Published on 22 2024. Downloaded on 18/10/24 08:09:28.
This article is licensed under a Creative Commons Attribution 3.0 Unported Licence.

acting as a flux.[167] They successfully synthesized $REBS_3$ in 2023. In the same year, Mao's group proposed another method to obtain $LaBS_3$ by employing $La_2S_3$, B, S, and $Li_2S$ as a flux and characterized its structure and NLO properties.[168]

$REBS_3$ (RE = La, Ce, Pr, Nd, Sm, and Tb) are isomorphic and adopt an orthorhombic $Pna2_1$ space group. $LaBS_3$ can serve as an example to discuss the crystal structure; as shown in Fig. 16, its structure comprises triangular $[BS_3]^{3-}$ units, with each La atom connecting to 9 S atoms to link with the $[BS_3]^{3-}$ units. Each $[BS_3]^{3-}$ unit is linked to 6 $La^{3+}$ atoms, ultimately forming the entire 3D network structure.

As expected, $LaBS_3$ possesses a large $E_g$ of 3.18 eV, the highest $d_{eff}$ among *ortho*-thioborates (1.2 × $AgGaS_2$ at 2050 nm), an ultra-high LIDT of 14 × $AgGaS_2$, a wide IR transmission range (0.35–25 μm), and exhibits PM behaviour. The results of theoretical calculations indicate that the $[LaS_9]^{15-}$ groups and the π-conjugated $[BS_3]^{3-}$ anions are the main sources of the SHG effect. In general, this research provides us with a new method to synthesize new NLO materials.

**2.3.2. $Ca_2RE(BS_3)(SiS_4)$ (RE = La, Ce, and Gd).** $Ca_2RE(BS_3)(SiS_4)$ (RE = La, Ce, and Gd) were synthesized by Mao's group in 2023 using a high-temperature solid-state reaction.[169] This represents the first case of thioborate–thiosilicates. The researchers employed a mixed flux method, utilizing BaS, CaS, $RE_2S_3$, $SiO_2$, B, and S as raw materials.

The compounds $Ca_2RE(BS_3)(SiS_4)$ (RE = La, Ce, and Gd) are isostructural and crystallize in the hexagonal $P6_3mc$ space group. Fig. 17 illustrates the structure of $Ca_2RE(BS_3)(SiS_4)$ along the *ab* plane. In this structure, the $RE^{3+}$ and $Ca^{2+}$ ions occupy the same site, referred to as the M site, with a ratio of 1/3 and 2/3, respectively. Each M site coordinates with 6 S atoms to form an $[MS_6]$ polyhedron, which connects with isolated $[BS_3]^{3-}$ and $[SiS_4]^{4-}$ units along the *c* axis, resulting in the overall 3D structure of $Ca_2RE(BS_3)(SiS_4)$.

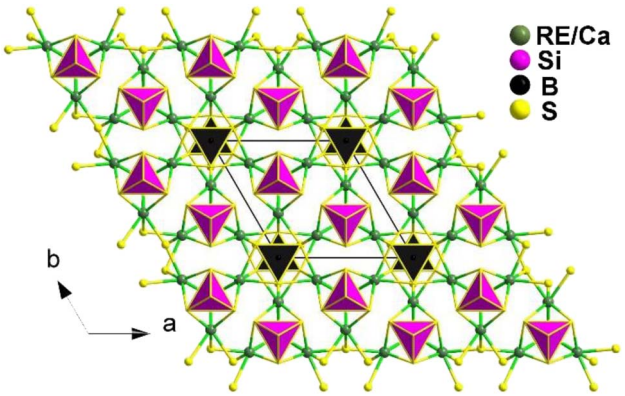


Fig. 17 Structure of $Ca_2RE(BS_3)(SiS_4)$ along the *ab* plane with the unit cell outlined.

Remarkably, all of them exhibit comprehensive properties that make them promising candidates for IR-NLO materials. These properties include strong PM $d_{eff}$ at 2050 nm (1.1–1.2 × $AgGaS_2$), high LIDTs (7–10 × $AgGaS_2$), a wide transmission range (0.45–11 μm), high thermal stabilities (>1073 K), and large calculated $\Delta n$ (0.126–0.149@1064 nm). These properties validate the material design strategy of combining $[BS_3]^{3-}$ and $[SiS_4]^{4-}$ NLO-active motifs.

Theoretical calculations indicate that the big $d_{eff}$ mainly stem from the synergy between the $[RES_6]$, $[BS_3]$, and $[SiS_4]$ groups. These findings not only expand the scope of research on chalcogenides but also offer a straightforward synthetic method for heteroanionic thioborates.

**2.3.3. $Eu_2P_2S_6$.** Compared with common metal chalcogenides, chalcogenophosphates with NCS structures are very few and difficult to synthesize, so they are rarely found as IR-NLO candidate materials. Although the crystal structure of RE-based chalcogenophosphate $Eu_2P_2S_6$ was reported as early as 1987,[170] its NLO performance was not reported by the Guo's research group until 2022.[171]

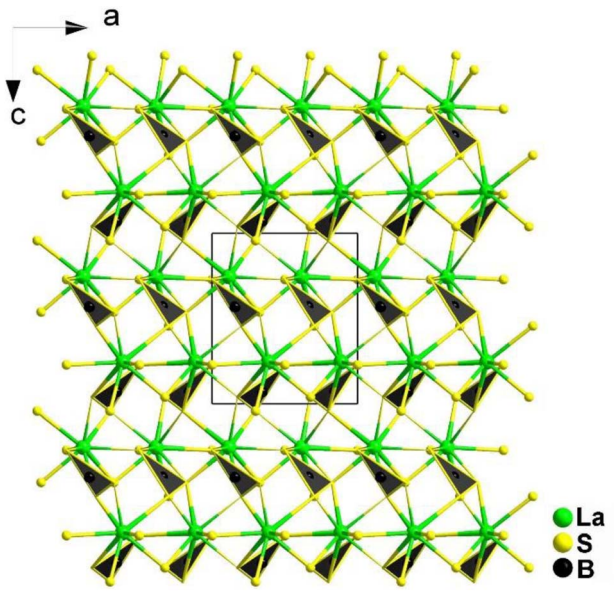


Fig. 16 Structure of $LaBS_3$ along the *ac* plane with the unit cell outlined.

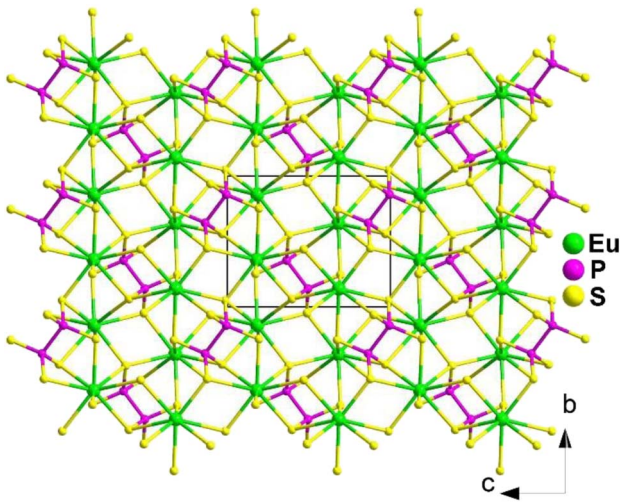


Fig. 18 Structure of $Eu_2P_2S_6$ along the *bc* plane with the unit cell outlined.

Open Access Article. Published on 22 2024. Downloaded on 18/10/24 08:09:28.
This article is licensed under a Creative Commons Attribution 3.0 Unported Licence.

Yellow block crystals of $Eu_2P_2S_6$ were prepared through a high-temperature solid-phase method between stoichiometric Eu, $P_2S_5$, and S at 1233 K. It belongs to the monoclinic *Pn* space group. The structure of $Eu_2P_2S_6$ can be viewed as comprising bicapped-triangular-prism [$EuS_8$] and dimeric [$P_2S_6$] functional primitives built into a 3D framework *via* 8 : 18 : 13 intergrowth (Fig. 18).

This first IR-NLO RE-based chalcogenophosphate, $Eu_2P_2S_6$, displays wonderful comprehensive optical properties, including a moderate PM $d_{eff}$ (0.9 × $AgGaS_2$), large LIDT (3.4 × $AgGaS_2$), and broad IR transparency region (0.49–15.4 μm). Based on the results of structural analysis and theoretical studies, the overall IR-NLO properties are attributable to the synergetic effect of [$EuS_8$] and [$P_2S_6$] functional primitives. This study not only developed the first RE-based chalcogenophosphate as an advanced NLO candidate, but also provided a representative example for the future discovery of high-performance RE-based IR-NLO chalcogenides.

**2.3.4. $KREP_2Se_6$ (RE = Sm, Tb, and Gd).** Combining the merits of multiple oxidation states, strong covalent character of the P–Q bonds, and low melting points, Guo's group successfully combined metal chalcophosphates with RE-centered units that exhibit large polarization, resulting in the synthesis of $KREP_2Se_6$ (RE = Sm, Tb, and Gd) in 2022.[172] The synthesis was carried out using the $M_xO_y$–B–Q (M = metal; Q = S, Se) solid-state route, which had previously been used to prepare chalcogenides by Huang and Guo *et al.*[108]

The first RE-based selenophosphates $KREP_2Se_6$ (RE = Sm, Tb, and Gd) belong to the monoclinic $P2_1$ space group. They are composed of a 2D $[REP_2Se_6]^-$ layer with $K^+$ ions filling the spaces in between (Fig. 19). The $[REP_2Se_6]^-$ layer is built by layers in which each bicapped-trigonal-prism [$RESe_8$] unit is linked to four [$RESe_8$] units by sharing edges and vertices. These [$RESe_8$] units also connect with 4 $[P_2Se_6]^{4-}$ units by sharing faces, edges, and corners. The co-vertices are arranged on one side, while the co-edges are arranged on the other.

As a result, $KREP_2Se_6$ (RE = Sm, Tb, and Gd) exhibit a PM $d_{eff}$ effect ranging from 0.34 to 1.08 × $AgGaS_2$ at 2100 nm and a LIDT ranging from 1.43 to 4.33 × $AgGaS_2$. The theoretical calculations suggest that the cooperation between [$P_2Se_6$] and [$RESe_8$] plays a predominant role in the $d_{eff}$. This research demonstrates that RE-based selenophosphates are a promising type of IR-NLO material. It not only enhances the understanding of crystal chemistry in RE-based chalcophosphates but also expands the range of potential applications for NLO materials.

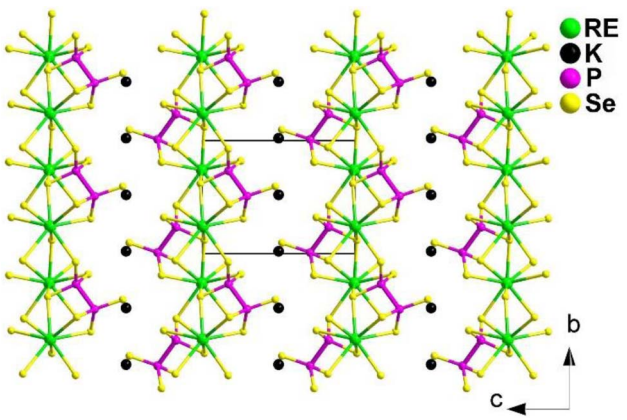


Fig. 19 Structure of $KREP_2Se_6$ along the *bc* plane with the unit cell outlined.

### 2.4. RE-based chalcohalides and oxychalcogenides

The emergence of heteroanions has enriched traditional functional units, as the differences in electronegativity result in a greater charge distribution shift within the interior of heteroanionic groups compared to conventional functional units.[215–228] This leads to distortions and the display of significant static dipole moments and anisotropy.[229–233] Unlike traditional chalcogenides, the presence of heteroanionic groups combines the high polarizability of chalcogenides with the advantages of oxides and halides that have wide $E_g$. RE-based chalcohalides and oxychalcogenides not only incorporate disparate anions but also feature the presence of salt-inclusion compounds. Below, eleven RE-based chalcohalides and oxychalcogenides are introduced.

**2.4.1. $La_6Cd_{0.75}Ga_2Q_{11.5}Cl_{2.5}$ (Q = S, Se).** Two novel quinary chalcohalides, $La_6Cd_{0.75}Ga_2Q_{11.5}Cl_{2.5}$ (Q = S, Se), with heteroanionic functional motifs were discovered in 2021 by Huang's group using $LaCl_3$ as a reaction-flux.[173] Both compounds belong to the NCS space group $P6_3$. Fig. 20a displays a schematic

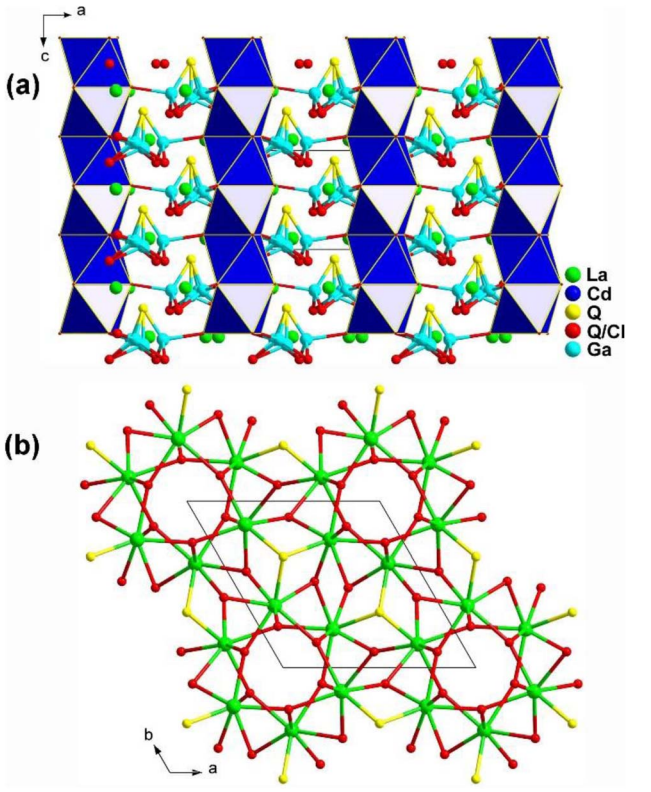


Fig. 20 Structure of (a) $La_6Cd_{0.75}Ga_2Q_{11.5}Cl_{2.5}$ along the *ac* plane and (b) 3D La/Q/(Q/Cl) network along the *ab* plane with the unit cell outlined.


© 2024 The Author(s). Published by the Royal Society of Chemistry

Open Access Article. Published on 22 2024. Downloaded on 18/10/24 08:09:28.
This article is licensed under a Creative Commons Attribution 3.0 Unported Licence.

diagram of $La_6Cd_{0.75}Ga_2Q_{11.5}Cl_{2.5}$ seen along the *ac* plane. In the structure, plane-linked 1D $[Cd(Q/Cl)_6]$ chains are packed along the $6_3$ axes, and the tetrahedral $[GaQ_4]$ units are separated along the direction of the 3-fold rotation axes. Furthermore, the $[La(Q/Cl)_6Q]$ polyhedra form a 3D network structure in the *ab* plane through vertex- and edge-sharing as shown in Fig. 20b with the unit cell outlined.

Moreover, the introduction of various heteroanionic functional motifs with varying sizes and electronegativity increases the distortion of structural groups while keeping the structural symmetry. This enhances the polarity of the NLO-active motifs, resulting in a greater $d_{eff}$. As expected, $La_6Cd_{0.75}Ga_2S_{11.5}Cl_{2.5}$ exhibits a large LIDT of 18.6 × $AgGaS_2$ @1064 nm and a strong $d_{eff}$ of 0.8 × $AgGaS_2$ @43–75 μm under 2050 nm laser irradiation.

**2.4.2. $RE_3AsS_5X_2$ (RE = La, Pr; X = Cl, Br).** The NCS chalcohalide $La_3AsS_5Br_2$ with the monoclinic space group *Cc* (no. 9),[174] which is isostructural to the previously reported $Pr_3AsS_5Cl_2$,[175] was successfully prepared using a salt flux growth method in 2023 by Wang's group.

The 3D network of $RE_3AsS_5X_2$ (RE = La, Pr; X = Cl, Br) is composed of $[RE1S_5X_3]$ bicapped trigonal prisms, $[RE2S_5X_3]$ bicapped trigonal prisms, $[RE3S_7]$ capped trigonal prisms, and SACLP $[AsS_3]$ trigonal pyramids, which are interconnected with each other (Fig. 21a). The coordination environment of the crystallographically independent RE atoms in the structure of $RE_3AsS_5X_2$ is provided in Fig. 21b. The electron localization function results confirmed that the arrangement of the $[AsS_3]$ groups contributes to the NCS nature of $RE_3AsS_5X_2$.

The moderate PM $d_{eff}$ (0.23 × $AgGaS_2$ @150–210 μm), easy growth of millimeter-sized crystals, excellent ambient stability, and wide $E_g$ (*ca.* 2.9 eV) of $La_3AsS_5Br_2$ suggest its potential applicability as an IR-NLO candidate.

**2.4.3. $Eu_{4.5}(B_5O_9)_2SI$.** The first sulfide borate to possess NLO activity, $Eu_{4.5}(B_5O_9)_2SI$, contains $I^-$, $S^{2-}$, and borate anions simultaneously. It was synthesized by Guo's group in 2019 as a derivative of $Eu_2B_5O_9S$ using KI as a flux in a solid-state reaction.[176] Both $Eu_{4.5}(B_5O_9)_2SI$ and $Eu_2B_5O_9S$ crystallize in the NCS orthorhombic *Pnn*2 space group, but $Eu_2B_5O_9S$ does not exhibit apparent SHG. Here, we discuss the structure of $Eu_{4.5}(B_5O_9)_2SI$ in detail.

The structure of $Eu_{4.5}(B_5O_9)_2SI$ along the *ab* plane is displayed in Fig. 22a. It consists of a 3D polyanionic network $\{(B_5O_9)^{3-}\}_\infty$, which is constructed by linking 3 $[BO_4]$ tetrahedra with 2 $[BO_3]$ planar triangles through shared O atoms. Along the *c* axis, there is a tubular accumulation $[Eu_2(B_5O_9)]_\infty$ framework built by $Eu_1$ and $Eu_2$ located in the cavities of the 3D network. The cavities of the 3D network are also occupied by $I^-$ ions. Fig. 22b shows the coordination environment of the crystallographically independent Eu atoms, which have three different coordination modes: $[Eu_1O_5S_2I]$, $[Eu_2O_5S_2I]$, and $[Eu_3O_4S_2]$.

The combination of $Eu^{2+}$, $S^{2-}$, $I^-$, and borates allows for the realization of a large $d_{eff}$ and a high LIDT. $Eu_{4.5}(B_5O_9)_2SI$ has an $E_g$ of 1.99 eV, a moderate $d_{eff}$ of 0.5 × $AgGaS_2$, a high LIDT of 15 × $AgGaS_2$, and PM behaviour. These results indicate that the Eu–S and B–O motifs play an important role in the $d_{eff}$ and offer an example of the practicality of this strategy.

**2.4.4. $(K_3I)[REB_{12}(GaS_4)_3]$ (RE = Sm, Gd).** The crystal structure of $(K_3I)[SmB_{12}(GaS_4)_3]$, which was reported by Guo's group in 2009, represents the first salt-inclusion chalcogenide

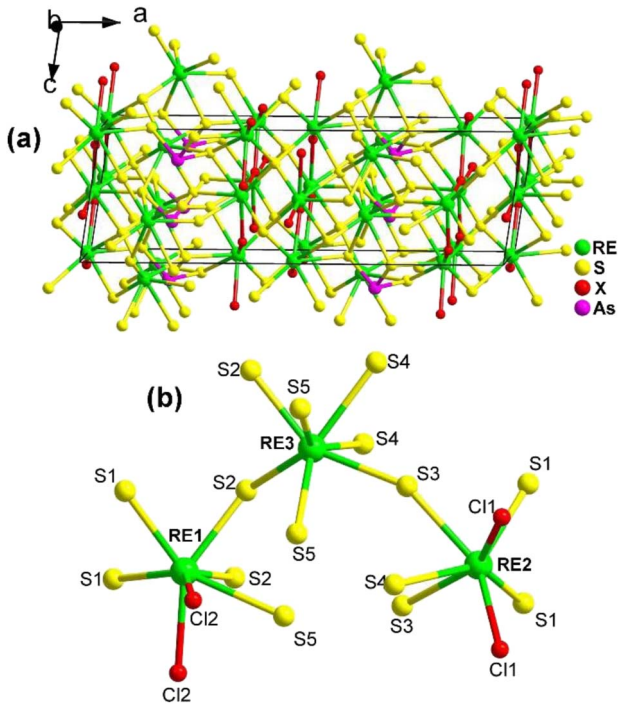


Fig. 21 Structure of (a) $RE_3AsS_5X_2$ along the *ac* plane with the unit cell outlined and (b) coordination environment of the crystallographically independent RE atoms.

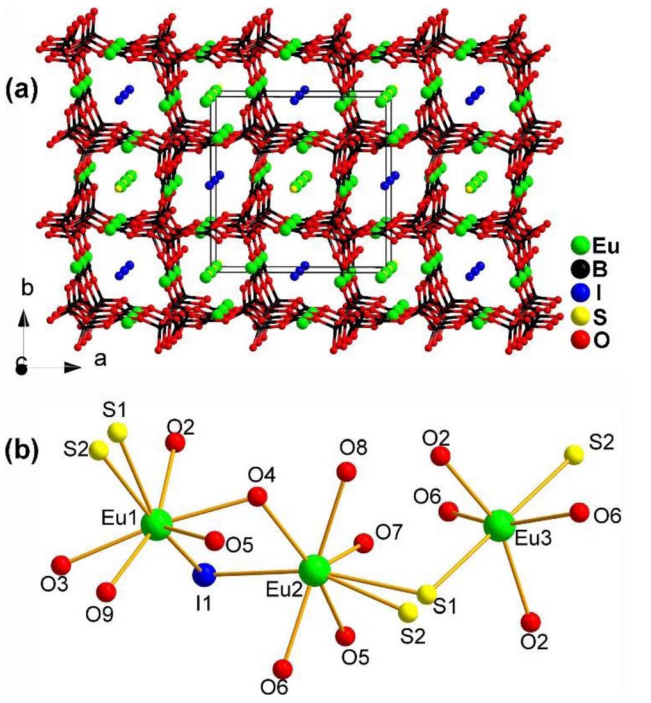


Fig. 22 Structure of (a) $Eu_{4.5}(B_5O_9)_2SI$ along the *ab* plane with the unit cell outlined and (b) coordination environment of the crystallographically independent Eu atoms.

Open Access Article. Published on 22 2024. Downloaded on 18/10/24 08:09:28.
This article is licensed under a Creative Commons Attribution 3.0 Unported Licence.

with NLO activity.[177] Throughout the next decade, multiple isomorphic compounds were synthesized using high-temperature solid-phase methods and various alkali-metal halide fluxes, with B being used in its original form.[234–236]

$(K_3I)[REB_{12}(GaS_4)_3]$ (RE = Sm, Gd) share the same structure and belong to the hexagonal chiral space group $P6_322$. In the asymmetric unit, there are 1 A, 1 X, 1 RE, 1 Ga, 2 B, and 2 Q positions. The crystal structure consists of two parts: the polycationic $[K_6I]^{5+}$ and the 3D open $[REB_{12}(GaS_4)_3]^{5-}$ anionic framework. The 3D framework comprises icosahedral $[B_{12}]$, tetrahedral $[GaS_4]$, and octahedral $[RES_6]$ functional primitives. Within the structure, the $[B_{12}]$ icosahedra are surrounded by 6 $[GaS_4]$ tetrahedra and consolidated by 2 $[RES_6]$ octahedra, resulting in a 3D honeycomb-like open framework. This framework forms channels occupied by face-sharing $[IK_6]$ octahedral chains along the *c* direction (see Fig. 23).

Due to the significantly low yield for most compounds, the majority of samples in this system were unable to undergo size-dependent SHG measurements. For instance, the $d_{eff}$ of $(K_3I)[SmB_{12}(GaS_4)_3]$ is approximately 0.3 times that of KDP when subjected to a 1940 nm laser. The small $d_{eff}$ can be attributed to the arrangement of the SHG-active groups in their structures, which hinders the improvement of macroscopic polarizabilities.

**2.4.5. $[RE_3S_2Cl_2][SbS_3]$ (RE = La, Ce) and $[La_3OSCl_2][SbS_3]$.** RE-based chalcohalide $[RE_3S_2Cl_2][SbS_3]$ (RE = La, Ce) and oxychalcogenide $[La_3OSCl_2][SbS_3]$ were reported by Zhao's research group in 2021[178] and 2022,[179] respectively. Although they show identical stoichiometry, they belong to different crystal systems and exhibit different structural symmetries.

$[RE_3S_2Cl_2][SbS_3]$ (RE = La, Ce) were obtained from a mixture of CsCl, RE, $GaCl_3$, $SbCl_3$, and S in a ratio of 1 : 4 : 1 : 1 : 5 using a high-temperature solid-state method at 1073 K. As shown in Fig. 24a, $[RE_3S_2Cl_2][SbS_3]$ belongs to the NCS *Cc* space group, where the 2D layers of $[RE_3S_2Cl_2]^{12+}$ arranged in the *bc* plane and the trigonal-pyramid $[SbS_3]$ motifs are stacked in an alternating pattern. However, the stacking of $[SbS_3]$ motifs in the crystal cell is in-phase and they are correlated with each other through the *n* sliding planes at $(x, 1/4, z)$. Unfortunately, no NLO performance has been reported for these two compounds.

Yellow crystals of $[La_3OSCl_2][SbS_3]$ were grown from a mixture of La, $LaCl_3$, Sb, $Sb_2O_3$, and S with a ratio of 7 : 2 : 1 : 1 : 12 at 1223 K. It can be seen as being obtained through partial isovalent anion substitution of the parent structure $[La_3S_2Cl_2][SbS_3]$. Interestingly, $[La_3OSCl_2][SbS_3]$ adopts the hexagonal space group $P6_3mc$, which is not isostructural with $[La_3S_2Cl_2][SbS_3]$ (monoclinic space group *Cc*), despite their having similar functional primitives. $[La_3OSCl_2][SbS_3]$ is made of 3D cationic $[La_3OSCl_2]^{3+}$ frameworks hosting covalent $[SbS_3]^{3-}$ motifs. The 3D cationic $[La_3OSCl_2]^{3+}$ are built *via* the 1D hexagonal columns of corner-sharing $[(Cl/S)La_3]$ polyhedra propagating along the $6_3$ axis situated in (0, 0, *z*) and $[OLa_3]$ trigonal pyramids through vertex-sharing. It is worth mentioning that experimental results indicate a moderate $d_{eff}$ (*ca.* 0.7 × $AgGaS_2$@50–100 μm) under a 2050 nm laser, and the calculated $\Delta n$ value is about 0.27 at 2050 nm, respectively.

**2.4.6. $YSeBO_2$.** Due to the difficulty of their synthesis, chalcogenide borates have been rarely studied as IR-NLO candidate materials in the past. The second selenide borate, $YSeBO_2$, was successfully discovered by Guo's group in 2020.[180] Transparent rodlike crystals of $YSeBO_2$ with a large $E_g$ of 3.45 eV were prepared through a traditional solid-phase reaction between $Y_2O_3$, $B_2O_3$, B, and Se and additional KI used as the flux.

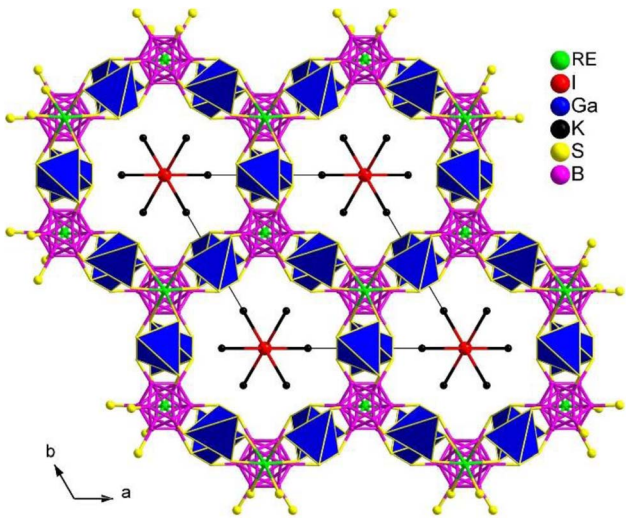


Fig. 23 Structure of $(K_3I)[REB_{12}(GaS_4)_3]$ with the unit cell outlined along the *ab* plane.

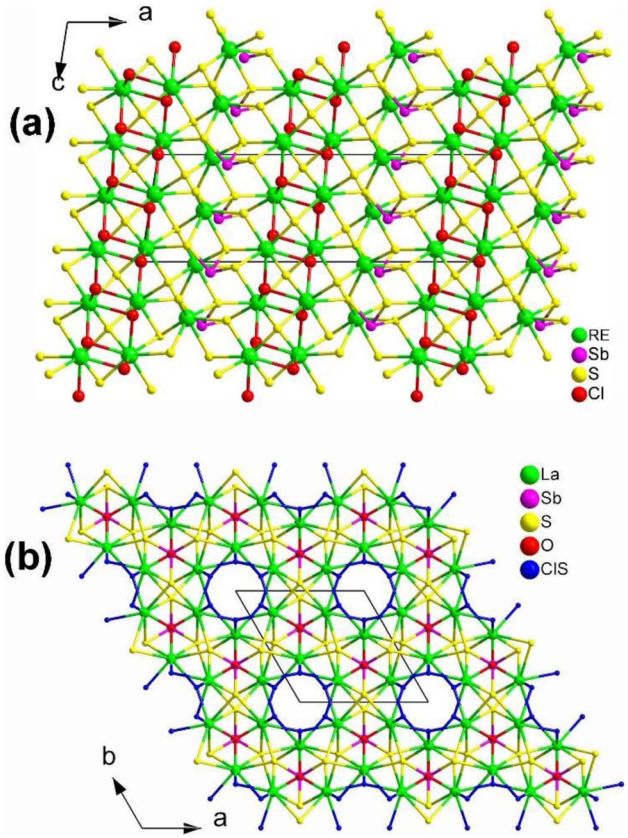


Fig. 24 Structures of (a) $[RE_3S_2Cl_2][SbS_3]$ along the *ac* plane and (b) $[La_3OSCl_2][SbS_3]$ along the *ab* plane with unit cell outlined.


© 2024 The Author(s). Published by the Royal Society of Chemistry

Open Access Article. Published on 22 2024. Downloaded on 18/10/24 08:09:28.
This article is licensed under a Creative Commons Attribution 3.0 Unported Licence.

$YSeBO_2$ adopts the orthorhombic polar space group $Cmc2_1$, and the 3D structure is formed by the connection between $[YO_3Se_4]^{11-}$ pentagonal bipyramids and $[BO_3]^{3-}$ planar triangles by sharing O edges (see Fig. 25). It is worth mentioning that the heteroanionic $[YO_3Se_4]^{11-}$ functional motif was first discovered in the chalcogenide system. In addition, $YSeBO_2$ displays a weak $d_{eff}$ of about 0.2 × KDP (@150–210 μm) with PM features. Theoretical analysis shows that the Se-4p and Y-4d states play a major role in the origin of SHG. The contribution of the $[BO_3]^{3-}$ planar triangles did not show any impact due to its unfavorable arrangement.

**2.4.7. $Eu_3GeOS_4$.** Using a mixed-anion strategy, Guo's group successfully obtained the first quaternary RE-based oxythiogermanate $Eu_3GeOS_4$ by introducing Eu and $[GeOS_3]$ in 2023.[181] The millimeter-size crystals of $Eu_3GeOS_4$ were prepared by using a traditional solid-state method at 1148 K.

$Eu_3GeOS_4$ belongs to the orthorhombic $Pca2_1$ space group. As displayed in Fig. 26, neighbouring $[EuOS_6]$ mono-capped trigonal prisms are interlinked through sharing faces to form a 3D framework structure, with isolated $[GeOS_3]$ tetrahedra occupying the cavities. In other words, without considering the Eu–O/S bonds, the crystal structure of $Eu_3GeOS_4$ can also be considered a pseudo-0D structure. It is interesting to note that the coordination mode of the heteroanionic $[EuOS_6]$ functional motif was discovered for the first time in oxychalcogenides.

$Eu_3GeOS_4$ not only shows an obvious $d_{eff}$ (0.24 × $AgGaS_2$@2050 nm), but also a large LIDT (8.86 × $AgGaS_2$@1064 nm). Theoretical calculations indicate that the $d_{eff}$ is attributed to the synergistic effect of the heteroanionic $[EuOS_6]$ and $[GeOS_3]$ functional motifs.

**2.4.8. $RE_3NbS_3O_4$ (RE = Ce, Sm, Gd, Dy).** A series of RE-based oxysulfides $RE_3NbS_3O_4$ (RE = Ce, Sm, Gd, Dy) were systemically investigated. Among them, the Sm and Gd compounds display NCS structures (space group: $Pna2_1$), while the Ce and Dy compounds exhibit CS structures (space group: *Pnma*), which is mainly caused by the various coordination types and stacking direction of Nb atoms as well as the different ionic radii of $RE^{3+}$ cations.[182–185]

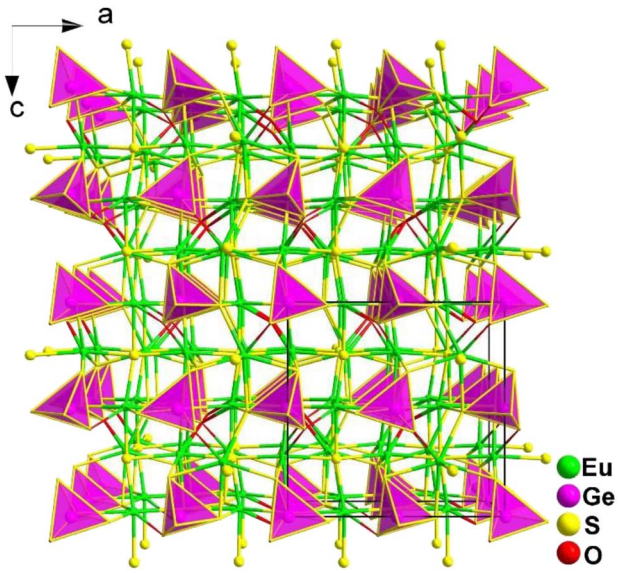


Fig. 26 Central projection of $Eu_3GeOS_4$ along the *ac* plane with the unit cell outlined.

The crystals of $RE_3NbS_3O_4$ were prepared through solid-phase reactions at 1273 K using $RE_2O_3$, $Nb_2O_5$, B, and S as the raw materials and excess KI as the flux. When charge-balanced $RE^{3+}$ cations are omitted, the NCS structure of $RE_3NbS_3O_4$ (RE = Sm, Gd) can be seen as a hexagonal cage formed by 6 Nb atoms encasing 6 RE atoms when viewed along the *bc* plane (see Fig. 27). Each RE forms two different coordination forms: a $[RES_4O_4]$ double-capped triangular prism and a $[RES_5O_3]$ dodecahedron.

$Sm_3NbS_3O_4$ and $Gd_3NbS_3O_4$ exhibit PM $d_{eff}$ of about 0.3 and 0.4 × $AgGaS_2$ under a 2100 nm laser and large LIDTs of 12.5 and

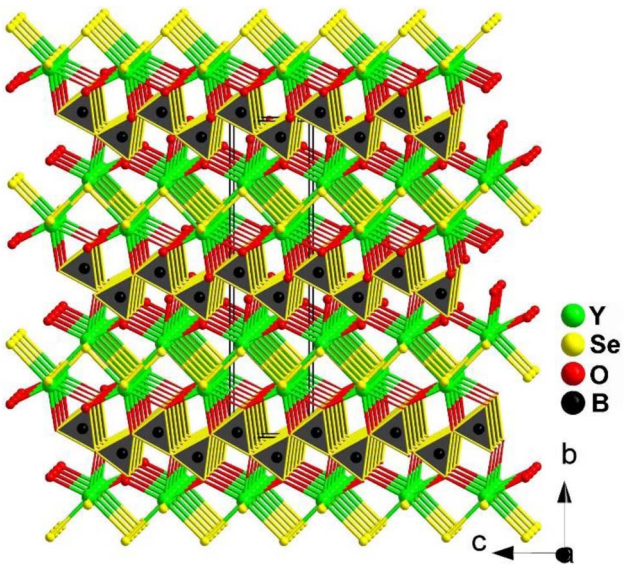


Fig. 25 Structure of $YSeBO_2$ along the *bc* plane with the unit cell outlined.

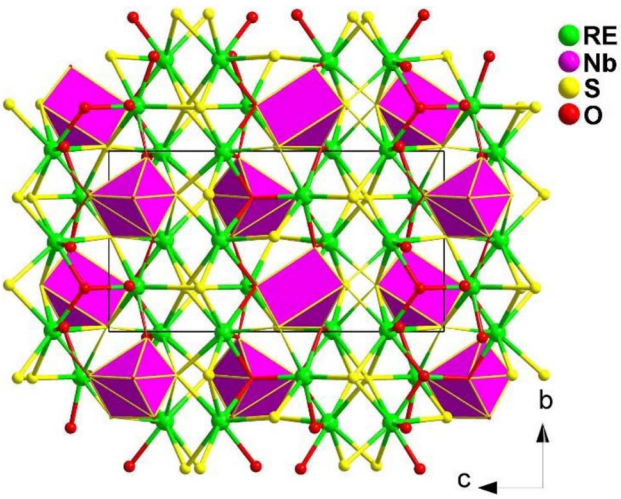


Fig. 27 Structure of $RE_3NbS_3O_4$ along the *bc* plane with the unit cell outlined.

Open Access Article. Published on 22 2024. Downloaded on 18/10/24 08:09:28.
This article is licensed under a Creative Commons Attribution 3.0 Unported Licence.

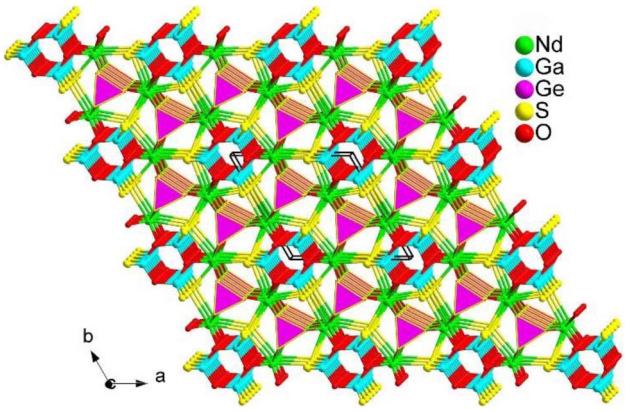


Fig. 28 Structure of $Nd_3[Ga_3O_3S_3][Ge_2O_7]$ along the *ab* plane with unit the cell outlined.

4.5 × $AgGaS_2$ at 1064 nm. The heteroanionic $[NbS_2O_4]$ unit was first found as a SHG-active motif, which offers a new route for discovering novel IR-NLO oxychalcogenides.

**2.4.9. $Nd_3[Ga_3O_3S_3][Ge_2O_7]$.** Previous studies have shown that it is challenging to achieve chalcogenides based on rare earth (RE) materials that have both a large band gap ($E_g$ > 3.5 eV) and a high effective nonlinear optical coefficient ($d_{eff}$ > 0.5 × $AgGaS_2$). However, in 2023, the Zhu research group successfully designed and synthesized a new RE-based oxychalcogenide, $Nd_3[Ga_3O_3][Ge_2O_7]$, for the first time.[186] This was achieved through a module substitution strategy using the parent structure $Cs_3[Sb_3O_6][Ge_2O_7]$.

$Nd_3[Ga_3O_3][Ge_2O_7]$ was discovered using the solid-phase method at 1273 K and adopts the hexagonal space group $P\bar{6}2c$ (no. 190). Its unique structure consists of three different modules: charge-balanced $Nd^{3+}$ cations, 0D $[Ge_2O_7]^{6-}$ dimers, and 1D $[Ga_3O_3S_3]^{3-}$ tubular chains (Fig. 28). The $Nd^{3+}$ cation is coordinated with O/S atoms to form a heteroligand $[NdO_6S_2]$ polyhedron. Experimental investigations of $Nd_3[Ga_3O_3][Ge_2O_7]$ demonstrate that it is the first RE-based IR-NLO oxychalcogenide, exhibiting excellent optical performance. This includes a strong $d_{eff}$ (*ca.* 0.8 × $AgGaS_2$@2050 nm), a large $E_g$ (*ca.* 4.35 eV) corresponding to an ultrahigh LIDT of 23 × $AgGaS_2$@1064 nm, a wide transparent window (0.25–13.7 μm), and good thermal stability (<1200 K).

Detailed theoretical results indicate that the remarkable $d_{eff}$ in $Nd_3[Ga_3O_3][Ge_2O_7]$ is mainly attributed to the cooperation of heteroanionic $[GaO_2S_2]$ and $[NdO_2S_6]$ functional motifs. This research not only expands the possibilities of IR-NLO families with heteroanionic motifs, but also offers a feasible strategy for the development of other high-performance IR-NLO systems.

**2.4.10. $Eu_2M^{II}Ge_2OS_6$ ($M^{II}$ = Mn, Fe, and Co).** By coupling RE elements with localized f-electrons, d-block transition metals with delocalized d-electrons, and the mixed anion group $[GeOS_3]$ with high polarizability, Guo's group successfully obtained the first melilite-type RE-based oxythiogermanates, $Eu_2M^{II}Ge_2OS_6$, where $M^{II}$ represents Mn, Fe, and Co, in 2023. These compounds were prepared *via* high-temperature solid-phase synthesis using KI as a flux.[187]

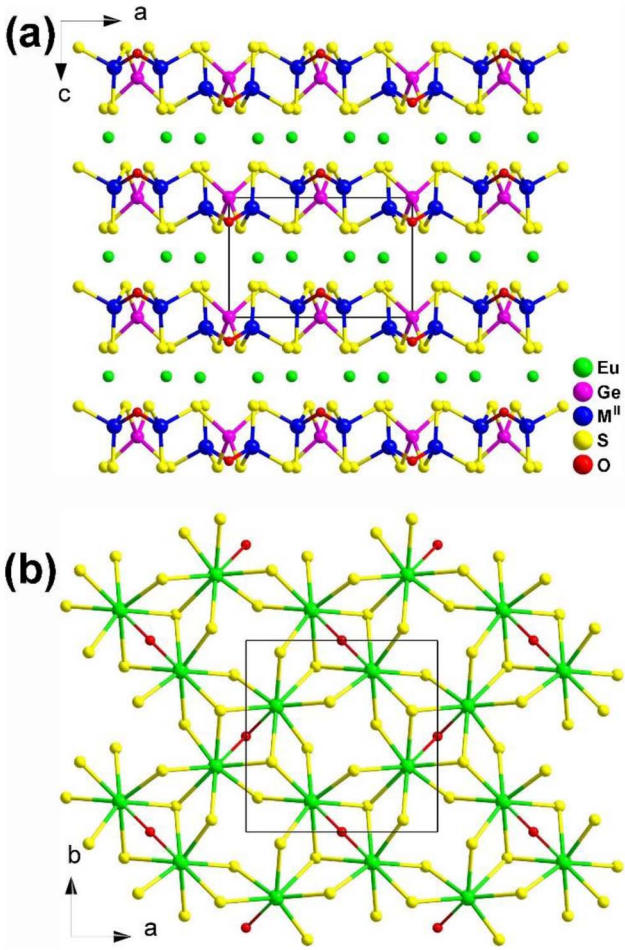


Fig. 29 Structure of (a) $Eu_2M^{II}Ge_2OS_6$ along the *ac* plane and (b) the 2D Eu/O/S network along the *ab* plane with the unit cell outlined.

$Eu_2M^{II}Ge_2OS_6$ ($M^{II}$ = Mn, Fe, and Co) are isomorphic and grow in a tetragonal NCS $P\bar{4}2_1m$ space group. As shown in Fig. 29a, two neighboring $[GeOS_3]$ tetrahedra build a dimer, $[Ge_2OS_6]$, by sharing an O atom. Each $[Ge_2OS_6]$ dimer then

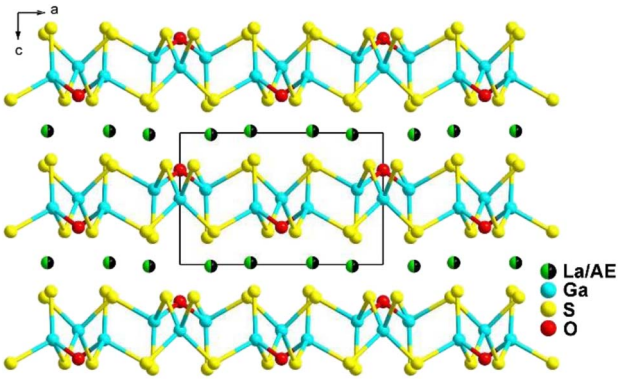


Fig. 30 Structure of $LaAEGa_3S_6O$ along the *ac* plane with the unit cell outlined.


© 2024 The Author(s). Published by the Royal Society of Chemistry

Open Access Article. Published on 22 2024. Downloaded on 18/10/24 08:09:28.
This article is licensed under a Creative Commons Attribution 3.0 Unported Licence.

interlinks with 4 $[M^{II}S_4]$ tetrahedra by sharing S corners, constructing corrugated 2D $[M^{II}Ge_2OS_6]^{4-}$ layers along the *ab* plane. The $[EuOS_7]$ bicapped trigonal prisms are located within these 2D interlayers and serve to bridge adjacent $[EuOS_7]$ together, forming the 3D network (Fig. 29b).

As a result, $Eu_2M^{II}Ge_2OS_6$ ($M^{II}$ = Mn, Fe, and Co) display excellent IR-NLO performance with an $E_g$ of 2.11–2.40 eV, a PM $d_{eff}$ of 0.3–0.5 × $AgGaS_2$ at 200–250 μm, and a large LIDT of 2.8–8.3 × $AgGaS_2$. They proposed that these compounds have the potential to replace $M^{II}$ using Cu or other d-block metals and other substitutions within the same family.

**2.4.11. $REAEGa_3S_6O$ (RE = La, Pr, and Nd; AE = Sr, Ca).** Recent studies have mainly focused on the individual performances of oxysulfides, but there has been little investigation into the comparisons in the specific properties and changes in a series of analogues including oxides, sulfides, and oxysulfides. In order to address this gap, a series of $REAEGa_3S_6O$ (RE = La, Pr, and Nd; AE = Sr, Ca) compounds were synthesized by Wu

Table 1 Summary of reported RE-based chalcogenides containing tetrahedral motifs

| Compound | $[REQ_n]$ polyhedra | Space group | $E_g$[a] (eV) | $d_{eff}$[b] (×$AgGaS_2$) | LIDT[b] (×$AgGaS_2$) | NPM/PM[c] | $\Delta n$[d] | Maximum temperature[f] | Ref. |
|---|---|---|---|---|---|---|---|---|---|
| $Dy_3GaS_6$ | $[DyS_7]$ | $Cmc2_1$ (no. 36) | 2.80 | 0.084 | 14 | PM | 0.068 | 1223 K | 69 |
| $Y_3GaS_6$ | $[YS_7]$ | $Cmc2_1$ (no. 36) | 2.88 | 0.21 | 18 | PM | 0.069 | 1223 K | 69 |
| $Ho_3GaS_6$ | $[HoS_7]$ | $Cmc2_1$ (no. 36) | 3.03 | 0.4 | N/A[e] | PM | 0.041 | 1223 K | 70 |
| $Er_3GaS_6$ | $[ErS_7]$ | $Cmc2_1$ (no. 36) | 3.08 | 0.6 | N/A | PM | 0.034 | 1223 K | 70 |
| $Eu_8Sn_4Se_{20}$ | $[EuSe_9]$ | $P2_12_12$ (no. 18) | 1.33 | 1 × α-$SiO_2$@150–210 μm | N/A | N/A | 0.16 | 1223 K | 72 |
| $EuCu_2GeSe_4$ | $[EuSe_8]$ | *Ama*2 (no. 40) | 1.74 | No signal | N/A | N/A | N/A | 1073 K | 75 |
| $EuCu_2GeS_4$ | $[EuSe_8]$ | $P3_221$ (no. 154) | 2.32 | No signal | N/A | N/A | N/A | 1073 K | 75 |
| $EuCu_2SiS_4$ | $[EuS_8]$ | $P3_121$ (no. 152) | 2.36 | No signal | N/A | N/A | N/A | 1073 K | 75 |
| $Dy_3Si_{0.85}Al_{0.53}S_7$ | $[DyS_8]$ | $P6_3$ (no. 173) | 2.03 | 1 × KTP@∼20 μm | N/A | N/A | N/A | 1223 K | 108 |
| $Dy_6Al_2SiS_{14}$ | $[DyS_8]$ | $P6_3$ (no. 173) | 2.22 | 2 × KTP@∼20 μm | N/A | N/A | N/A | 1223 K | 108 |
| $Sm_3Al_{0.33}SiS_7$ | $[SmS_8]$ | $P6_3$ (no. 173) | 2.26 | 0.3 × KDP@∼150 μm | N/A | N/A | N/A | 1223 K | 108 |
| $Y_6ZnSi_2S_{14}$ | $[YS_8]$ | $P6_3$ (no. 173) | 2.38 | 0.84@∼20 μm | N/A | N/A | N/A | 1223 K | 108 |
| $La_3GaGe_{0.5}S_7$ | $[LaS_8]$ | $P6_3$ (no. 173) | 2.54 | 4.8@74–106 μm | N/A | NPM | 0.023 | 1223 K | 82 |
| $Sm_3GaGe_{0.5}S_7$ | $[SmS_8]$ | $P6_3$ (no. 173) | 2.50 | Weak | N/A | N/A | N/A | 1253 K | 82 |
| $La_3CuGeSe_7$ | $[LaSe_8]$ | $P6_3$ (no. 173) | 2.00 | 0.3 × $SiO_2$ | N/A | N/A | N/A | 1073 K | 94 |
| $La_3LiSnS_7$ | $[LaS_8]$ | $P6_3$ (no. 173) | 2.40 | 1.2 | 2.5 | PM | 0.031 | 1073 K | 126 |
| $Sm_3LiSiS_7$ | $[SmS_8]$ | $P6_3$ (no. 173) | 2.83 | 1.5 @88–105 μm | 3.7 | NPM | N/A | 1373 K | 124 |
| $La_3LiGeS_7$ | $[LaS_8]$ | $P6_3$ (no. 173) | 3.02 | 0.7 | 6.0 | PM | 0.025 | 1173 K | 126 |
| $La_6Ga_2GeS_{14}$ | $[LaS_8]$ | $P6_3$ (no. 173) | 2.54 | 4.8@74–106 μm | N/A | NPM | 0.023 | 1223 K | 82 |
| $La_6In_2GeS_{14}$ | $[LaS_8]$ | $P6_3$ (no. 173) | 2.61 | 1.8@74–106 μm | N/A | NPM | 0.007 | 1173 K | 82 |
| $Y_6Ga_2GeS_{14}$ | $[YS_8]$ | $P6_3$ (no. 173) | 2.30 | Weak | 3.0 | NPM | N/A | 1153 K | 130 |
| $EuHgGeSe_4$ | $[EuSe_8]$ | *Ama*2 (no. 40) | 1.97 | 3.1 | N/A | PM | 0.31 | 1173 K | 133 |
| $EuHgSnS_4$ | $[EuS_8]$ | *Ama*2 (no. 40) | 2.14 | 1.77 | N/A | PM | 0.33 | 1173 K | 133 |
| $EuCdGeSe_4$ | $[EuSe_8]$ | *Ama*2 (no. 40) | 2.25 | 3.8 | N/A | PM | 0.18 | 1273 K | 132 |
| $EuCdGeS_4$ | $[EuS_8]$ | *Ama*2 (no. 40) | 2.50 | 2.6 | N/A | PM | 0.18 | 1273 K | 132 |
| $Eu_2Ga_2GeS_7$ | $[EuS_6]$ | $P\bar{4}2_1m$ (no. 113) | 2.30 | 1.6@46–74 μm | N/A | NPM | 0.098 | 1123 K | 134 |
| $La_2Ga_2GeS_8$ | $[LaS_8]$ | $Cmc2_1$ (no. 36) | 2.78 | weak@46–74 μm | N/A | N/A | 0.077 | 1373 K | 134 |
| $Ba_2InYSe_5$ | $[YSe_6]$ | $Cmc2_1$ (no. 36) | 2.31 | 1 × $AgGaSe_2$ | N/A | N/A | N/A | 1323 K | 135 |
| $Ba_4Sm_2Cd_3S_{10}$ | $[SmS_6]$ | $Cmc2_1$ (no. 36) | 2.77 | 1.8@46–74 μm | 14.3 | N/A | 0.044 | 1173 K | 137 |
| $LaSrGa_3S_7$ | $[LaS_8]$ | $P\bar{4}2_1m$ (no. 113) | 2.92 | 1.3 | 5.0 | PM | 0.099 | 1273 K | 139 |
| $LaCaGa_3S_7$ | $[LaS_8]$ | $P\bar{4}2_1m$ (no. 113) | 2.96 | 1.3 | 5.0 | PM | 0.134 | 1273 K | 139 |
| $LaCaAl_3S_7$ | $[LaS_8]$ | $P\bar{4}2_1m$ (no. 113) | 3.76 | 0.8 | 9 | PM | 0.059 | 1473 K | 138 |
| $LaSrAl_3S_7$ | $[LaS_8]$ | $P\bar{4}2_1m$ (no. 113) | 3.78 | 1.1 | 9 | PM | 0.077 | 1473 K | 138 |
| $La_2Ca_3Sn_3S_{12}$ | $[(La/Ca)S_7]/[(La/Ca)S_9]$ | $P\bar{4}2m$ (no. 189) | 1.65 | 1.4@200–250 μm | N/A | NPM | 0.008 | 1073 K | 142 |
| $Sm_2CaSn_3S_{12}$ | N/A | $P\bar{4}2m$ (no. 189) | 1.66 | 1.2@200–250 μm | N/A | NPM | N/A | 1073 K | 142 |
| $Gd_2Ca_3Sn_3S_{12}$ | N/A | $P\bar{4}2m$ (no. 189) | 1.63 | 1.0@200–250 μm | N/A | NPM | N/A | 1073 K | 142 |
| $La_2Sr_3Sn_3S_{12}$ | $[(La/Ca)S_7]/[(La/Ca)S_8]$ | $Pmc2_1$ (no. 26) | 1.68 | 3.0 | N/A | PM | 0.086 | 1073 K | 142 |
| $Sm_2Sr_3Sn_3S_{12}$ | N/A | $Pmc2_1$ (no. 26) | 1.71 | 2.5 | N/A | PM | N/A | 1073 K | 142 |
| $Gd_2Sr_3Sn_3S_{12}$ | N/A | $Pmc2_1$ (no. 26) | 1.51 | 2.6 | N/A | PM | N/A | 1073 K | 142 |
| $CeLiSiS_4$ | $[CeS_8]$ | *Ama*2 (no. 40) | 2.92 | 2.1 | 9 | PM | 0.054 | 1073 K | 143 |
| $LaLiSiS_4$ | $[LaS_8]$ | *Ama*2 (no. 40) | 3.71 | 2.0 | 14 | PM | 0.033 | 1073 K | 143 |
| $CsLaGeS_4$ | $[LaS_7]$ | $P2_12_12_1$ (no. 19) | 3.60 | 0.5 × α-$SiO_2$ | N/A | N/A | N/A | 1173 K | 146 |
| $KYGeS_4$ | $[YS_7]$ | $P2_1$ (no. 4) | 3.15 | 1.0 | 10 | PM | 0.12 | 1173 K | 148 |
| $K_3YP_2S_8$ | $[YS_8]$ | $P2_1$ (no. 4) | 3.37 | 1.4 | 7.0 | PM | 0.096 | 923 K | 149 |
| $K_3HoP_2S_8$ | $[HoS_8]$ | $P2_1$ (no. 4) | N/A | 1.1 | 3.0 | PM | 0.084 | 923 K | 149 |
| $K_3ErP_2S_8$ | $[ErS_8]$ | $P2_1$ (no. 4) | N/A | 1.2 | 2.5 | PM | 0.099 | 923 K | 149 |

[a] Experimental value. [b] Powder sample. [c] PM = phase-matchability, NPM = nonphase-matchability. [d] Theoretical value. [e] N/A = not available. [f] The maximum temperature of solid-state reaction.

Open Access Article. Published on 22 2024. Downloaded on 18/10/24 08:09:28.
This article is licensed under a Creative Commons Attribution 3.0 Unported Licence.

Table 2 Summary of reported RE-based chalcogenides containing lone-pair-electron motifs[e]

| Compound | [REQ$_n$] polyhedra | Space group | $E_g$[a] (eV) | $d_{eff}$[b] (×AgGaS$_2$) | LIDT[b] (×AgGaS$_2$) | NPM/PM[c] | $\Delta n$[d] | Maximum temperature[f] | Ref. |
|---|---|---|---|---|---|---|---|---|---|
| $Ce_8Sb_2S_{15}$ | [$CeS_7$]/[$CeS_8$] | $I4_1cd$ (no. 110) | 1.99 | 0.03 | N/A | NPM | N/A | 1223 K | 163 |
| $La_8Sb_2S_{15}$ | [$LaS_7$]/[$LaS_8$] | $I4_1cd$ (no. 110) | 2.30 | 1.2@74–106 μm | N/A | NPM | N/A | 1223 K | 171 |
| $La_2CuSbS_5$ | [$LaS_8$]/[$LaS_{10}$] | $Ima2$ (no. 46) | 2.06 | 0.5 | 6.7 | PM | 0.11 | 1273 K | 154 |
| $La_4InSbS_9$ | [$LaS_6$]/[$LaS_7$] | $P4_12_12$ (no. 92) | 2.07 | 1.5 | N/A | PM | N/A | 1223 K | 156 |
| $Pr_4InSbS_9$ | [$PrS_6$]/[$PrS_7$] | $P4_32_12$ (no. 96) | 2.09 | No signal | N/A | N/A | N/A | 1223 K | 156 |
| $Nd_4InSbS_9$ | [$NdS_6$]/[$NdS_7$] | $P4_32_12$ (no. 96) | 2.12 | No signal | N/A | N/A | N/A | 1223 K | 156 |
| $Sm_4InSbS_9$ | [$SmS_6$]/[$SmS_7$] | $P4_32_12$ (no. 96) | 2.13 | 0.75@150–210 μm | N/A | PM | N/A | 1223 K | 158 |
| $Y_4GaSbS_9$ | [$YS_6$]/[$YS_7$] | $Aba2$ (no. 41) | 2.06 | 7.5 × α-$SiO_2$@74–106 μm | N/A | NPM | N/A | 1223 K | 159 |
| $Sm_4GaSbS_9$ | [$SmS_6$]/[$SmS_7$] | $Aba2$ (no. 41) | 2.23 | 3.8@46–74 μm | N/A | NPM | N/A | 1223 K | 157 |
| $Ho_4GaSbS_9$ | [$HoS_6$]/[$HoS_7$] | $Aba2$ (no. 41) | 2.25 | 0.25@46–74 μm | N/A | N/A | N/A | 1223 K | 157 |
| $Gd_4GaSbS_9$ | [$GdS_6$]/[$GdS_7$] | $Aba2$ (no. 41) | 2.41 | 0.8@46–74 μm | N/A | NPM | N/A | 1223 K | 157 |
| $Tb_4GaSbS_9$ | [$TbS_6$]/[$TbS_7$] | $Aba2$ (no. 41) | 2.44 | Weak | N/A | N/A | N/A | 1223 K | 157 |

[a] Experimental value. [b] Powder sample. [c] PM = phase-matchability, NPM = nonphase-matchability. [d] Theoretical value. [e] N/A = not available. [f] The maximum temperature of solid-state reaction.

Table 3 A summary of reported RE-based chalcogenides containing [$BS_3$] and [$P_2Q_6$] motifs[e]

| Compound | [REQ$_n$] polyhedra | Space group | $E_g$[a] (eV) | $d_{eff}$[b] (×AgGaS$_2$) | LIDT (×AgGaS$_2$)[b] | NPM/PM[c] | $\Delta n$[d] | Maximum temperature[f] | Ref. |
|---|---|---|---|---|---|---|---|---|---|
| $LaBS_3$ | [$LaS_9$] | $Pna2_1$ (no. 33) | 3.18 | 1.2 | 14 | PM | 0.143 | 1023 K | 167 |
| $Ca_2La(BS_3)(SiS_4)$ | [$LaS_6$] | $P6_3mc$ (no. 186) | 3.38 | 1.1 | 10 | PM | 0.149 | 1123 K | 169 |
| $Ca_2Ce(BS_3)(SiS_4)$ | [$CeS_6$] | $P6_3mc$ (no. 186) | 2.65 | 1.2 | 7 | PM | 0.149 | 1123 K | 169 |
| $Ca_2Gd(BS_3)(SiS_4)$ | [$GdS_6$] | $P6_3mc$ (no. 186) | 3.20 | 1.1 | 8 | PM | 0.126 | 1123 K | 169 |
| $Eu_2P_2S_6$ | [$EuS_8$] | $Pc$ (no. 7) | 2.54 | 0.9 | 3.4 | PM | 0.074 | 1223 K | 171 |
| $KSmP_2Se_6$ | [$SmSe_8$] | $P2_1$ (no. 4) | 1.92 | 1.08 | 1.43 | PM | N/A | 1023 K | 172 |
| $KTbP_2Se_6$ | [$TbSe_8$] | $P2_1$ (no. 4) | 2.46 | 0.35 | 2.29 | PM | N/A | 1023 K | 172 |
| $KGdP_2Se_6$ | [$GdSe_8$] | $P2_1$ (no. 4) | 2.53 | 0.44 | 4.33 | PM | 0.081 | 1023 K | 172 |

[a] Experimental value. [b] Powder sample. [c] PM = phase-matchability, NPM = nonphase-matchability. [d] Theoretical value. [e] N/A = not available. [f] The maximum temperature of solid-state reaction.

and co-works in 2022, along with their corresponding $LaAEGa_3O_7$ oxides and $LaAEGa_3S_7$ sulfides, which served as reference materials.[128] The aim was to systematically study the trends in the key properties from oxides to sulfides to oxysulfides.

All of the $REAEGa_3S_6O$ oxysulfides belong to the $P\bar{4}2_1m$ space group of the tetragonal system, and they are isostructural with $LaAEGa_3O_7$ and $LaAEGa_3S_7$. Fig. 30 presents the unique structure of these compounds, which can be described as consisting of two functional modules: charge-balanced $[RE/AE]^{5+}$ cations and 2D $[Ga_3S_6O]^{5-}$ Cairo pentagonal layers. The charge-balanced module is composed of [(RE/AE)$S_7$O] groups that are connected through edge- and face-sharing interactions, forming a 2D [(RE/AE)$S_7$O]$_n$ layer. On the other hand, the 2D layers can be seen as a combination of many 5-membered rings, with two [$GaS_4$] and three [$GaS_3O$] units surrounding each ring.

In particular, $REAEGa_3S_6O$ fulfills the property balance requirements (*e.g.*, wide $E_g$: 3.21–3.27 eV and PM $d_{eff}$: 0.9–1.0 × $AgGaS_2$). This compound shows promise as a potential IR-NLO crystal, as it combines the advantages of $LaAEGa_3O_7$ and $LaAEGa_3S_7$ through heteroanion-oriented performance engineering. The structure–activity relationships reveal that the heteroanionic [(RE/AE)$S_7$O] and [$GaS_3O$] functional motifs are particularly promising for NLO activity, as they exhibit large cooperation in the origin of SHG. These findings not only provide a clear understanding of the variation in properties from oxide to sulfide to oxysulfide, but also highlight the feasibility of using heteroanion-oriented design to develop novel NLO candidates with well-balanced performances.

## 3. Conclusions and perspectives

RE-based chalcogenides, with their unique electronic configurations, have been extensively discussed in the field of IR-NLO for several decades, and there has been growing interest in recent years. According to incomplete statistics, there are over 400 compounds with non-centrosymmetric structures among RE-based chalcogenides. However, to date, there has not been a comprehensive review that systematically summarized these compounds. Therefore, this paper provided a summary analysis of their synthesis methods, structures, optical properties, and structure–property relationships. The results of the statistical analysis of these compounds are summarized in Tables 1–4 and Schemes 1–4. Additionally, some key findings have been uncovered:

(1) Due to the Gd discontinuity effect, there is a slight variation in the ionic radius of lanthanide elements, which leads to differences in their chemical and physical properties.


© 2024 The Author(s). Published by the Royal Society of Chemistry

Open Access Article. Published on 22 2024. Downloaded on 18/10/24 08:09:28.
This article is licensed under a Creative Commons Attribution 3.0 Unported Licence.

Table 4 A summary of reported RE-based chalcohalides and oxychalcogenide[e]

| Compound | $[REQ_n]$ polyhedra | Space group | $E_g$ (eV)[a] | $d_{eff}$ ($\times AgGaS_2$)[b] | LIDT ($\times AgGaS_2$)[b] | NPM/PM[c] | $\Delta n$[d] | Maximum temperature[f] | Ref. |
|---|---|---|---|---|---|---|---|---|---|
| $La_6Cd_{0.75}Ga_2Se_{11.5}Cl_{2.5}$ | $[LaSe_7]$ | $P6_3$ (no. 173) | 1.65 | 0.1@43–75 μm | N/A | NPM | N/A | 1173 K | 173 |
| $La_6Cd_{0.75}Ga_2S_{11.5}Cl_{2.5}$ | $[LaS_7]$ | $P6_3$ (no. 173) | 2.28 | 0.8@43–75 μm | 18.6 | NPM | N/A | 1173 K | 173 |
| $La_3AsS_5Br_2$ | $[LaS_7]$ | $Cc$ (no. 9) | 2.90 | 0.23 | N/A | N/A | N/A | 1123 K | 174 |
| $Eu_{4.5}(B_5O_9)_2SI$ | $[EuO_5S_2I]/[EuO_3S_2I]/[EuO_4S_2]$ | $Pnn2$ (no. 34) | 1.99 | 0.5 | 15 | PM | N/A | 1223 K | 176 |
| $(K_3I)[SmB_{12}(GaS_4)_3]$ | $[SmS_6]$ | $P6_322$ (no. 182) | 2.35 | 0.3 × KTP | N/A | N/A | N/A | 1223 K | 177 |
| $[La_3OSCl_2][SbS_3]$ | $[(Cl/S)La_3]$ | $P6_3mc$ (no. 186) | 2.50 | 0.7 | N/A | N/A | 0.269 | 1223 K | 178 |
| $YSeBO_2$ | $[YO_3Se_4]^{11-}$ | $Cmc2_1$ (no. 36) | 3.45 | 0.0054 | N/A | PM | N/A | 1223 K | 180 |
| $Eu_3GeOS_4$ | $[EuOS_6]$ | $Pca2_1$ (no. 29) | 2.05 | 0.24@110–150 μm | 8.86 | NPM | 0.019 | 1148 K | 181 |
| $Sm_3NbS_3O_4$ | $[SmS_8]$ | $Pna2_1$ (no. 33) | 2.68 | 0.3 | 12.5 | PM | N/A | 1273 K | 185 |
| $Gd_3NbS_3O_4$ | $[GdS_8]$ | $Pna2_1$ (no. 33) | 2.74 | 0.4 | 4.5 | PM | N/A | 1273 K | 185 |
| $Nd_3[Ga_3O_3S_3][Ge_2O_7]$ | $[NdO_6S_2]$ | $P\bar{4}2c$ (No. 190) | 4.35 | 0.8 | 23 | PM | 0.091 | 1273 K | 186 |
| $Eu_2MnGe_2OS_6$ | $[EuOS_7]$ | $P\bar{4}2_1m$ (no. 113) | 2.40 | 0.3 | 8.3 | PM | 0.13 | 1173 K | 187 |
| $Eu_2FeGe_2OS_6$ | $[EuOS_7]$ | $P\bar{4}2_1m$ (no. 113) | 2.11 | 0.3 | 2.8 | PM | N/A | 1173 K | 187 |
| $Eu_2CoGe_2OS_6$ | $[EuOS_7]$ | $P\bar{4}2_1m$ (no. 113) | 2.14 | 0.5 | 3.2 | PM | N/A | 1173 K | 187 |
| $LaSrGa_3S_6O$ | $[LaS_7O]$ | $P\bar{4}2_1m$ (no. 113) | 3.21 | 1.0 | 14 | PM | 0.138 | 1273 K | 139 |
| $LaCaGa_3S_6O$ | $[LaS_7O]$ | $P\bar{4}2_1m$ (no. 113) | 3.27 | 0.9 | 14 | PM | 0.163 | 1273 K | 139 |

[a] Experimental value. [b] Powder sample. [c] PM = phase-matchability, NPM = nonphase-matchability. [d] Theoretical value. [e] N/A = not available. [f] The maximum temperature of solid-state reaction.

Therefore, based on differences in electronic configuration, as well as physical and chemical properties, the elements preceding Gd are classified as light RE elements or cerium-group elements (La–Eu), while the remaining elements are classified as heavy RE elements (Gd–Lu, Y, and Sc). As shown in Scheme 1, light RE-based chalcogenide compounds have greater appeal than heavy ones. Based on the classification of light and heavy RE elements, an analysis of these compounds reveals that the probability of obtaining NCS compounds through the synthesis of light RE elements is 47.9% (excluding the radioactive *Pm* element), which is twice the average of heavy RE elements (20.0%). Furthermore, the NLO-active compounds in the light RE elements group account for a remarkable 70.7% of the total, which is also double the percentage found in the heavy group (29.3%). Of course, the price difference between light and heavy RE elements will also impact the synthesis and amount of research into the compounds. However, a more profound reason might be that the synthesis of light RE elements is more conducive to obtaining NCS structures and exhibiting NLO activity. Moreover, by statistically analysing the NCS compounds of each RE element and specifically examining those with NLO activity, it is observed that the top three elements are Eu (88.2%), La (38.2%), and Sm (29.7%), which all belong to the light RE category. Additionally, the percentage of NLO-active materials among Eu-based NCS materials is remarkably high, reaching 88.2%, surpassing the second-ranked La (38.2%). This demonstrates that among the 16 elements (excluding the radioactive *Pm*), Eu-based compounds stand out as promising candidates for IR-NLO materials with excellent potential.

(2) These compounds can be divided into four categories based upon the number of elements: ternary (9, 10.6%), quaternary (62, 72.9%), quinary (13, 15.3%), and hexanary (1, 1.2%). Furthermore, in terms of the dimensionality of the crystal structure, there are 6 (7.1%) 0D compounds, 1 (1.2%) 1D compound, 22 2D (25.9%) compounds, 42 (49.4%) 3D compounds, and 14 (16.5%) MD compounds. Additionally, based on the crystal systems, they can be divided into five categories: monoclinic (12, 14.1%), orthorhombic (31, 36.5%), tetragonal (16, 18.8%), trigonal (2, 2.4%), and hexagonal (24, 28.2%). Analysis of the space group distribution revealed that

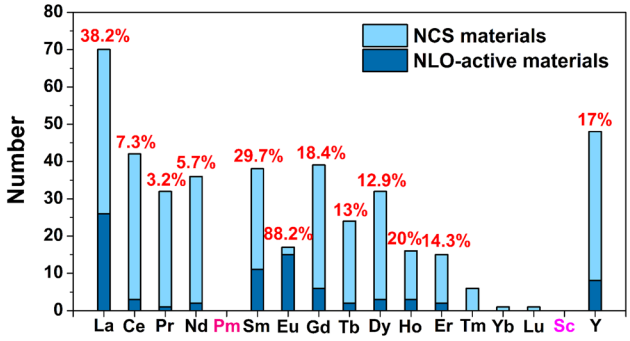


Scheme 1 Distribution and proportion of NLO activity in different RE-based NCS materials.

Open Access Article. Published on 22 2024. Downloaded on 18/10/24 08:09:28.
This article is licensed under a Creative Commons Attribution 3.0 Unported Licence.

the top three space groups are $P6_3$ (No.173, 15 examples), $Cmc2_1$ (No.36, 11 examples), and $P\bar{4}2_1m$ (no. 113, 10 examples) (see Scheme 2 for details).

(3) The RE-based asymmetric building motifs that have been reported currently exhibit two different coordination modes. These include the single-anion coordination mode, which comprises [REQ$_n$] ($n$ = 6–10), and the heteroanion coordination mode, which consists mainly of [REQ$_2$O$_4$], [REQ$_4$O$_3$], [REQ$_6$O], [REQ$_7$O], [REQ$_2$O$_6$], [REQ$_4$OX$_3$], and [REQ$_2$O$_5$X] (Scheme 3). It is important to note that the structures of these asymmetric building motifs determine their performance. Consequently, RE-based materials composed of these different asymmetric building motifs exhibit distinct IR-NLO properties. In Scheme 4, a comparison of the $d_{eff}$ and $E_g$ of RE-based IR-NLO materials is displayed. $La_6Ga_2GeS_{14}$ has the largest $d_{eff}$ of 4.8 × $AgGaS_2$ at a particle size of 74–106 μm among all the RE-based chalcogenide IR-NLO materials, but it has a relatively small $E_g$ of 2.54 eV. $Nd_3[Ga_3O_3S_3][Ge_2O_7]$ has the largest $E_g$ of 4.35 eV, while it has a relatively small $d_{eff}$ of 0.8 × $AgGaS_2$ at a particle size of 150–210 μm. The "performance-balanced area" indicates the potential materials whose $d_{eff}$ and $E_g$ are both higher than those of $AgGaS_2$. In this performance-balanced area, there are 11 PM chalcogenides, but only 1 PM oxychalcogenide and no chalcohalides, which demonstrates the outstanding performance of RE-based chalcogenides. The exploration of oxychalcogenides and chalcohalides should be continued to enable a more in-depth analysis of their

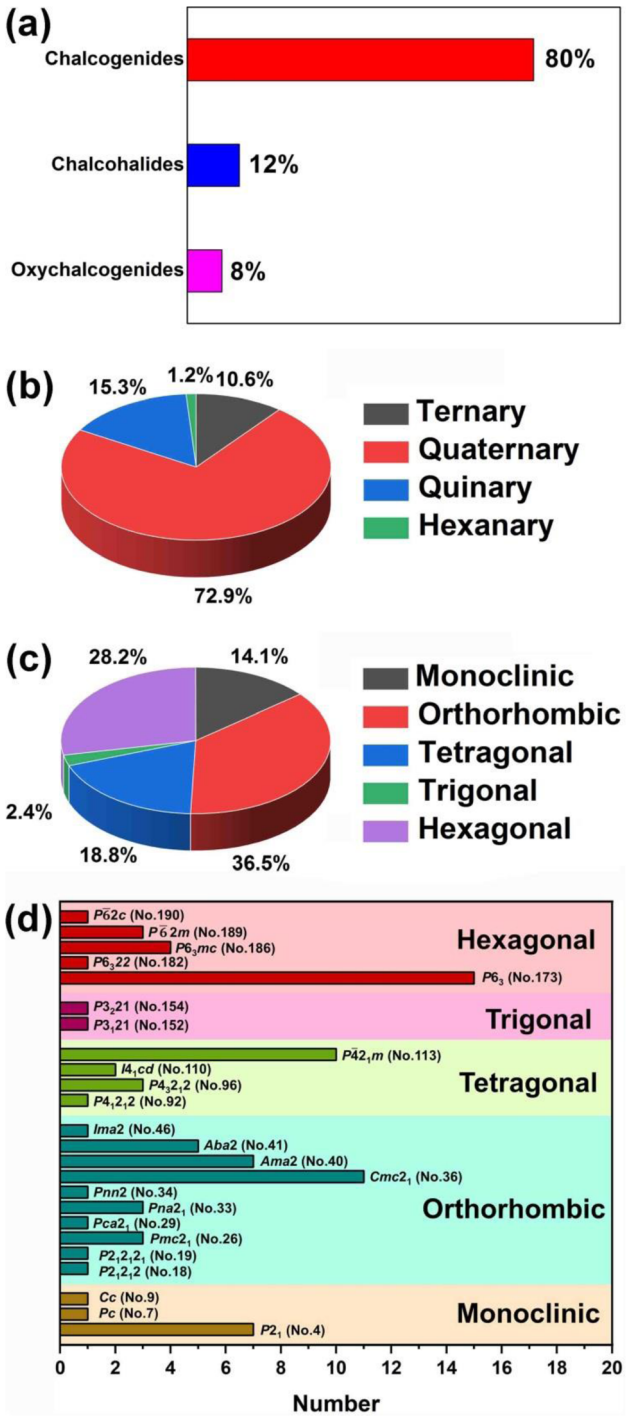


Scheme 2 Distributions of RE-based IR-NLO materials based on (a and b) chemical composition, (c) crystal system, and (d) the space groups in five crystal systems.

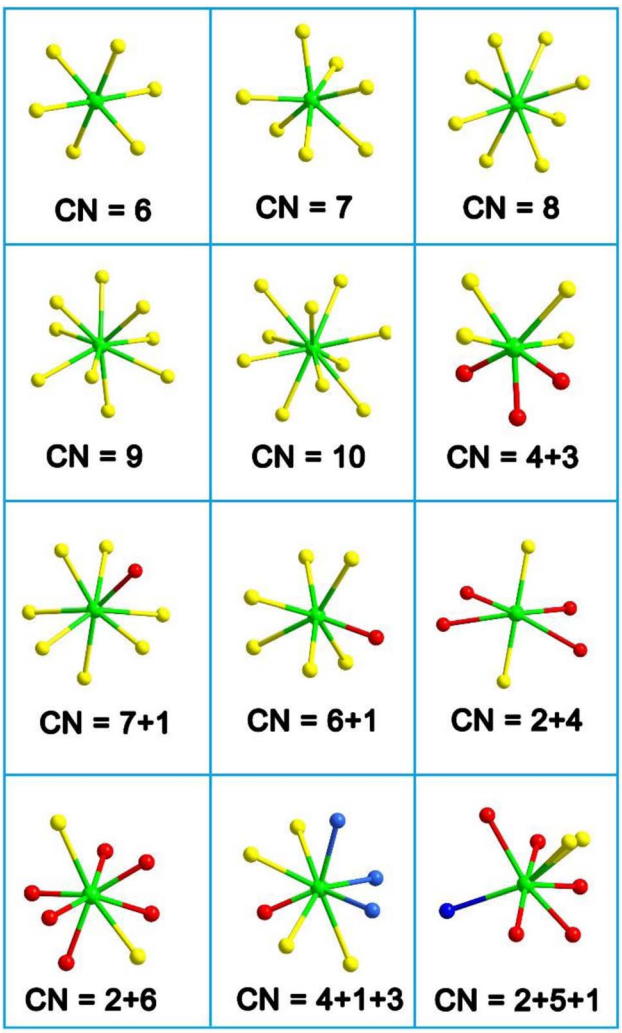


Scheme 3 Coordination modes of RE-based asymmetric building motifs (CN = coordination number). Green atom: RE; yellow atom: chalcogen (Q); red atom: O; blue atom: halogen (X).


© 2024 The Author(s). Published by the Royal Society of Chemistry

Open Access Article. Published on 22 2024. Downloaded on 18/10/24 08:09:28.
This article is licensed under a Creative Commons Attribution 3.0 Unported Licence.

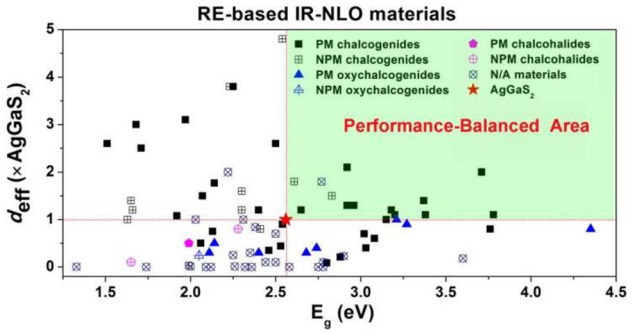


Scheme 4 Comparison of the $d_{eff}$ (×$AgGaS_2$) and $E_g$ (eV) for selected RE-based materials with IR-NLO properties (the green shaded region represents the performance-balanced area, wherein $d_{eff}$ > 1.0 $AgGaS_2$ and $E_g$ > 2.56 eV).

structural chemistry and understanding the origin of their properties through additional experimental results.

(4) For the synthesis method of RE-based IR-NLO compounds, the common method is high-temperature solid-state synthesis. Additionally, the introduction of RE elements not only involves the use of elemental RE, but also employs the reactive flux and boron–chalcogen mixture methods. The boron–chalcogen mixture method uses boron and RE oxides to remove oxygen *in situ* from rare earth oxides during the reaction, allowing the participation of RE elements. The emergence of this method enriches the selection of reaction pathways.

Currently, out of over 400 RE-based compounds, fewer than 100 demonstrate NLO properties. With decades of accumulated knowledge, our predecessors have laid a substantial foundation for us. Now is the opportune moment to strategically delve into synthesizing and exploring the underlying mechanisms, cultivating the soil to harvest successful outcomes. For this, the following outlook is provided:

(1) Further investigation into the mechanisms of RE-based polyhedra is needed. Currently, a significant question remains unanswered in the realm of RE-based compounds: why do only certain compounds of RE elements exhibit nonlinear effects in isomeric compounds? The differences among RE cations go beyond simple considerations of atomic radius; the underlying reasons should be attributed to variations in their electronic structures. Previous researchers have explored and synthesized numerous compounds in this field. In-depth studies of the electronic structures of different cations can help to uncover the answer to this question. Additionally, the contribution of the 5d and 4f empty orbitals of RE cations plays a crucial role in the conductive bands. By delving into the electronic structures of various anions and selectively substituting RE cations and anions with different 4f and 5d electronic structures based on their distinct structures, blind synthesis of RE-based compounds can be avoided, and hidden treasures within the accumulated knowledge can be uncovered. In contemporary research, the continual progress in theoretical calculations and machine learning plays a pivotal role in the exploration and design of novel materials. When synthesizing RE-based chalcogenides, the substitutability of RE sites with various RE elements is commonly considered, yet synthesis endeavours are often time-consuming. Consequently, upon successfully synthesizing a particular compound, it becomes important to validate, through theoretical calculations, the generalizability of the synthesis method to other RE elements. Additionally, when investigating isostructural compounds, a judicious approach involves preliminary theoretical analyses to identify RE elements that may exhibit superior performance, guiding subsequent synthesis explorations.

(2) According to Pauling's third and fourth rules, in systems containing more than one type of cation, polyhedra with high oxidation states and low coordination numbers tend to be connected through sharing corners or remain unconnected. The two functional motifs $[PS_4]$ and $[SiS_4]$, which are beneficial in terms of $E_g$, can be taken as examples. Due to the high positive charge and low coordination of the central cations, self-aggregation into high-dimensional frameworks becomes challenging under electrostatic rules. Therefore, a common approach for stabilization is to connect them with other polyhedra possessing central cations with lower positive charges and higher coordination. When alkali earth metals or alkali metals bond with these functional motifs, the resulting bonds are primarily ionic in nature. One characteristic of ionic bonds is isotropy, which makes it difficult to restrict the orientation of functional motifs and thus facilitates the formation of a thermodynamically stable centrosymmetric phase. Additionally, the isotropic nature of these bonds leads to low optical anisotropy. The bonding between $RE^{n+}$ and $S^{2-}$ is complex, primarily due to the complexity of their respective electronic structures. Furthermore, as different $RE^{n+}$ engage in bonding, the variability in their individual electronic structures contributes to distinct electron density of states within the system. As a result, this diversity leads to varying responses to external light stimuli. The presence of high-coordination RE cations acts as a binder between polyhedra with high oxidation states and coordination numbers. In these systems, RE cations not only play a role as a structural binder, but also contribute to providing nonlinear optical responses. Therefore, re-examining the structures of different compounds in the database reveals that introducing RE cations to connect previously disordered functional units may have a rejuvenating effect of "old wood meets spring", enhancing performance while adjusting the structure.

(3) The growth of large crystals is necessary. Currently, the major RE-based compounds are tested in the powder state, but the real working state of crystal materials is the single-crystal state. Consequently, in order to satisfy the demands of test accuracy, further test results are needed in the large single-crystal state, which is also a prerequisite for evaluating the commercialization of NLO materials.

## Data availability

There is no experimental or computational data associated with this article.

## Author contributions

Ping Feng: investigation, writing – original draft. Jia-Xiang Zhang: investigation, writing – original draft. Mao-Yin Ran:

investigation, formal analysis. Xin-Tao Wu: conceptualization, formal analysis. Hua Lin: supervision, conceptualization, writing – review & editing. Qi-Long Zhu: supervision, writing – review & editing.

## Conflicts of interest

There are no conflicts to declare.

## Acknowledgements

This work was sponsored by the National Natural Science Foundation of China (22175175), Fujian Science & Technology Innovation Laboratory for Optoelectronic Information of China (2021ZR118), and the Natural Science Foundation of Fujian Province (2022L3092 and 2023H0041).

## Notes and references

1 D. F. Voss, *Science*, 1987, **237**, 573.
2 J. C. Whitehead, *Nature*, 1998, **393**, 430.
3 S. W. Eaton, A. Fu, A. B. Wong, C.-Z. Ning and P. Yang, *Nat. Rev. Mater.*, 2016, **1**, 16028.
4 N. T. Otterstrom, R. O. Behunin, E. A. Kittlaus, Z. Wang and P. T. Rakich, *Science*, 2018, **360**, 1113.
5 N. Ahn, C. Livache, V. Pinchetti and V. I. Klimov, *Chem. Rev.*, 2023, **123**, 8251.
6 T. Schneider, *Nonlinear Optics in Telecommunications*, Springer Science & Business Media, 2004.
7 D. N. Nikogosyan, *Nonlinear Optical Crystals: A Complete Survey*, Springer, New York, 1st edn, 2005.
8 M. G. Papadopoulos, A. J. Sadlej and J. Leszczynski, *Nonlinear optical properties of matter*, Springer, 2006.
9 C. T. Chen, T. Sasaki, R. K. Li, Y. C. Wu, Z. S. Lin and Y. Mori, *Nonlinear Optical Borate Crystals: Principals and Applications*, John Wiley & Sons, 2012.
10 A. Newell, *Nonlinear Optics*, CRC Press, 2018.
11 P. S. Halasyamani and J. M. Rondinelli, *Nat. Commun.*, 2018, **9**, 2972.
12 M. Mutailipu, M. Zhang, H. Z. Yang and L. S. Pan, *Acc. Chem. Res.*, 2019, **52**, 791.
13 M. Mutailipu and S. Pan, *Angew. Chem., Int. Ed.*, 2020, **59**, 20302.
14 Y. C. Liu, Y. G. Shen, S. G. Zhao and J. H. Luo, *Coord. Chem. Rev.*, 2020, **407**, 213152.
15 M. Mutailipu, K. R. Poeppelmeier and L. S. Pan, *Chem. Rev.*, 2021, **121**, 1130.
16 J. Chen, C.-L. Hu, F. Kong and J.-G. Mao, *Acc. Chem. Res.*, 2021, **54**, 2775.
17 X. H. Meng, W. L. Yin and M. J. Xia, *Coord. Chem. Rev.*, 2021, **439**, 213916.
18 H. Fan, N. Ye and M. Luo, *Acc. Chem. Res.*, 2023, **56**, 3099.
19 X. Liu, Y.-C. Yang, M.-Y. Li, L. Chen and L.-M. Wu, *Chem. Soc. Rev.*, 2023, **52**, 8699.
20 J.-X. Zhang, P. Feng, M.-Y. Ran, X.-T. Wu, H. Lin and Q.-L. Zhu, *Coord. Chem. Rev.*, 2024, **505**, 215617.
21 R. C. Eckardt, H. Masuda, Y. X. Fan and R. L. Byer, *IEEE J. Quantum Electron.*, 1990, **26**, 922.
22 M. E. Hagerman and K. R. Poeppelmeier, *Chem. Mater.*, 1995, **7**, 602.
23 Y. N. Xia, C. T. Chen, D. Y. Tang and B. C. Wu, *Adv. Mater.*, 1995, **7**, 79.
24 C. T. Chen, B. C. Wu, A. D. Jiang and G. M. You, *Sci. Sin., Ser. B*, 1985, **28**, 235.
25 A. Harasaki and K. Kato, *Jpn. J. Appl. Phys.*, 1997, **36**, 700.
26 G. C. Catella, L. R. Shiozawa, J. R. Hietanen, R. C. Eckardt, R. K. Route, R. S. Feigelson, D. G. Cooper and C. L. Marquardt, *Appl. Opt.*, 1993, **32**, 3948.
27 G. D. Boyd, E. Buehler and F. G. Storz, *Appl. Phys. Lett.*, 1971, **18**, 301.
28 L. Kang, D. M. Ramo, Z. Lin, P. D. Bristowe, J. Qin and C. Chen, *J. Mater. Chem. C*, 2013, **1**, 7363–7370.
29 R. He, H. Huang, L. Kang, W. Yao, X. Jiang, Z. Lin, J. Qin and C. Chen, *Appl. Phys. Lett.*, 2013, **102**, 231904.
30 Z. Lin, X. Jiang, L. Kang, P. Gong, S. Luo and M. H. Lee, *J. Phys. D: Appl. Phys.*, 2014, **47**, 253001.
31 F. Liang, L. Kang, Z. Lin and Y. Wu, *Cryst. Growth Des.*, 2017, **17**, 2254.
32 G. Peng, Y. Yang, Y. H. Tang, M. Luo, T. Yan, Y. Zhou, C. Lin, Z. Lin and N. Ye, *Chem. Commun.*, 2017, **53**, 9398.
33 C. Hu, B. Zhang, B.-H. Lei, S. Pan and Z. Yang, *ACS Appl. Mater. Interfaces*, 2018, **10**, 26413.
34 Z. Yang, B.-H. Lei, W. Zhang and S. Pan, *Chem. Mater.*, 2019, **31**, 2807.
35 J. Yu, B. Zhang, X. Zhang, Y. Wang, K. Wu and M.-H. Lee, *ACS Appl. Mater. Interfaces*, 2020, **12**, 45023.
36 B.-W. Liu, X.-M. Jiang, S.-M. Pei, W.-F. Chen, L.-Q. Yang and G.-C. Guo, *Mater. Horiz.*, 2021, **8**, 3394.
37 H. Li, J. Min, Z. Yang, Z. Wang, S. Pan and A. R. Oganov, *Angew. Chem., Int. Ed.*, 2021, **60**, 10791.
38 L. Xiong, L.-M. Wu and L. Chen, *Angew. Chem., Int. Ed.*, 2021, **60**, 25063.
39 L. Kang, M. L. Zhou, J. Y Yao, Z. S. Lin, Y. C Wu and C. T. Chen, *J. Am. Chem. Soc.*, 2015, **137**, 13049.
40 F. Liang, L. Kang, Z. S. Lin, Y. C. Wu and C. T. Chen, *Coord. Chem. Rev.*, 2017, **333**, 57.
41 J.-R. Xiao, S.-H. Yang, F. Feng, H.-G. Xue and S.-P. Guo, *Coord. Chem. Rev.*, 2017, **347**, 23.
42 M.-M. Chen, H.-G. Xue and S.-P. Guo, *Coord. Chem. Rev.*, 2018, **368**, 115.
43 P. Gong, F. Liang, L. Kang, X. Chen, J. Qin, Y. Wu and Z. Lin, *Coord. Chem. Rev.*, 2019, **380**, 83.
44 L. Kang, F. Liang, X. Jiang, Z. Lin and C. Chen, *Acc. Chem. Res.*, 2020, **53**, 209.
45 K. Wu, Y. Yang and L. Gao, *Coord. Chem. Rev.*, 2020, **418**, 213380.
46 L. Gao, J. Huang, S. Guo, Z. Yang and S. Pan, *Coord. Chem. Rev.*, 2020, **421**, 213379.
47 G. Zou and K. M. Ok, *Chem. Sci.*, 2020, **11**, 5404.
48 J. Dang, D. Mei, Y. Wu and Z. Lin, *Coord. Chem. Rev.*, 2021, **431**, 213692.
49 F. Hou, D. Mei, M. Xia and Y. Wu, *Coord. Chem. Rev.*, 2021, **444**, 214038.

Open Access Article. Published on 22 2024. Downloaded on 18/10/24 08:09:28.
This article is licensed under a Creative Commons Attribution 3.0 Unported Licence.


© 2024 The Author(s). Published by the Royal Society of Chemistry

Open Access Article. Published on 22 2024. Downloaded on 18/10/24 08:09:28.
This article is licensed under a Creative Commons Attribution 3.0 Unported Licence.

50 C. X. Li, X. H. Meng, Z. Li and J. Y. Yao, *Coord. Chem. Rev.*, 2022, **453**, 214328.
51 X. L. Chen and K. M. Ok, *Chem. Sci.*, 2022, **13**, 3942.
52 H.-D. Yang, M.-Y. Ran, W.-B. Wei, X.-T. Wu, H. Lin and Q.-L. Zhu, *Mater. Today Phys.*, 2023, **35**, 101127.
53 M.-Y. Ran, A.-Y. Wang, W.-B. Wei, X.-T. Wu, H. Lin and Q.-L. Zhu, *Coord. Chem. Rev.*, 2023, **481**, 215059.
54 R. G. Pearson, *J. Am. Chem. Soc.*, 1963, **85**, 3533.
55 I. Chung and M. G. Kanatzidis, *Chem. Mater.*, 2014, **26**, 849.
56 C. L. Hu and J. G. Mao, *Coord. Chem. Rev.*, 2015, **288**, 1.
57 S.-P. Guo, Y. Chi and G.-C. Guo, *Coord. Chem. Rev.*, 2017, **335**, 44.
58 K. Wu and S. L. Pan, *Coord. Chem. Rev.*, 2018, **377**, 191.
59 Y. Y. Li, W. J. Wang, H. Wang, H. Lin and L. M. Wu, *Cryst. Growth Des.*, 2019, **19**, 4172.
60 J. Zhao, D. Mei, W. Wang, Y. Wu and D. Xue, *J. Rare Earths*, 2021, **39**, 1455.
61 Y. F. Shi, W. B. Wei, X. T. Wu, H. Lin and Q. L. Zhu, *Dalton Trans.*, 2021, **50**, 4112.
62 H. Chen, W.-B. Wei, H. Lin and X.-T. Wu, *Coord. Chem. Rev.*, 2021, **448**, 214154.
63 H.-D. Yang, M.-Y. Ran, W.-B. Wei, X.-T. Wu, H. Lin and Q.-L. Zhu, *Chem.–Asian J.*, 2021, **16**, 3299.
64 H. Chen, M.-Y. Ran, W.-B. Wei, X.-T. Wu, H. Lin and Q.-L. Zhu, *Coord. Chem. Rev.*, 2022, **470**, 214706.
65 Z.-X. Chen, W. Liu and S.-P. Guo, *Coord. Chem. Rev.*, 2023, **474**, 214870.
66 J. J. Xu and K. Wu, *Coord. Chem. Rev.*, 2023, **486**, 215139.
67 P.-F. Li, J.-G. Mao and F. Kong, *Mater. Today Phys.*, 2023, **37**, 101197.
68 A. M. Lozac'h, S. Jaulmes and M. Guittard, *C. R. Acad. Sci., Ser. C*, 1971, **272**, 1123.
69 M. J. Zhang, B. X. Li, B. W. Liu, Y. H. Fan, X. G. Li, H. Y. Zeng and G. C. Guo, *Dalton Trans.*, 2013, **42**, 14223.
70 H. Y. Chen, Y. Y. Zhang, Y. F. Yang and S. P. Guo, *J. Alloys Compd.*, 2021, **868**, 1873.
71 C. R. Evenson IV and P. K. Dorhout, *Z. Anorg. Allg. Chem.*, 2001, **627**, 2178.
72 S. H. Yang, X. H. Li, W. D. Yao, Q. T. Xu and S. P. Guo, *J. Solid State Chem.*, 2020, **288**, 1095.
73 J. Llanos, C. Mujica, V. Sánchez and O. Peña, *J. Solid State Chem.*, 2003, **173**, 78.
74 J. A. Aitken, J. W. Lekse, J.-L. Yao and R. Quinones, *J. Solid State Chem.*, 2009, **182**, 141.
75 Z. D. Sun, Y. Chi and S. P. Guo, *J. Solid State Chem.*, 2019, **269**, 225.
76 F. Q. Huang and J. A. Ibers, *Acta Crystallogr., Sect. C*, 1999, **55**, 1210.
77 L. D. Gulay, O. S. Lychmanyuk, J. Stepien-Damm, A. Pietraszko and I. D. Olekseyuk, *J. Alloys Compd.*, 2005, **402**, 201.
78 I. Hartenbach, A. C. Mueller and T. Schleid, *Z. Anorg. Allg. Chem.*, 2006, **632**, 2147.
79 L. D. Gulay, O. S. Lychmanyuk, I. D. Olekseyuk, M. Daszkiewicz, J. Stepien-Damm and A. Pietraszko, *J. Alloys Compd.*, 2007, **431**, 185.
80 M. Daszkiewicz, L. D. Gulay, A. Pietraszko and V. Y. Shemet, *J. Solid State Chem.*, 2007, **180**, 2053.
81 I. Hartenbach, T. Nilges and T. Schleid, *Z. Anorg. Allg. Chem.*, 2007, **633**, 24452.
82 Y. F. Shi, Y. K. Chen, M. C. Chen, L. M. Wu, H. Lin, L. J. Zhou and L. Chen, *Chem. Mater.*, 2015, **27**, 1876.
83 A. Michelet and J. Flahaut, *C. R. Acad. Sci. Ser. C*, 1969, **269**, 1203.
84 G. Perez, M. Darriet-Duale and P. Hagenmuller, *J. Solid State Chem.*, 1970, **2**, 42.
85 G. Perez and M. Darriet, *C. R. Acad, Sci. Ser. C*, 1970, **270**, 420.
86 M. Guittard and M. Julienpo, *Bull. Soc. Chim. Fr.*, 1970, **7**, 2467.
87 G. Collin and J. Flahaut, *C. R. Acad. Sci. Ser. C.*, 1970, **270**, 488.
88 Y. Q. Zhou, A. K. Iyer, A. O. Oliynyk, M. Heyberger, Y. X. Lin, Y. Qiu and A. Mar, *J. Solid State Chem.*, 2019, **278**, 120914.
89 M. A. Agaev, V. O. Aliev, A. B. Agaev and E. V. Magerramov, *Inorg. Mater.*, 1994, **30**, 1423.
90 S. J. Hwu, C. K. Bucher, J. D. Carpenter and S. P. Taylor, *Inorg. Chem.*, 1995, **34**, 1979.
91 R. L. Gitzendanner, C. M. Spencer, F. J. DiSalvo, M. A. Pell and J. A. Ibers, *J. Solid State Chem.*, 1996, **131**, 399.
92 S. H. Lin, J. G. Mao, G. C. Guo and J. S. Huang, *J. Alloys Compd.*, 1997, **252**, 8.
93 Y. T. Yang and J. A. Ibers, *J. Solid State Chem.*, 2000, **155**, 433.
94 K. M. Poduska, F. J. DiSalvo, K. Min and P. S. Halasyamani, *J. Alloys Compd.*, 2002, **335**, L5.
95 I. Hartenbach and T. Schleid, *J. Solid State Chem.*, 2003, **171**, 382.
96 L. D. Gulay, I. D. Olekseyuk, M. Wolcryz and J. Stepien-Damm, *Z. Anorg. Allg. Chem.*, 2005, **631**, 1919.
97 L. D. Gulay and I. D. Olekseyuk, *J. Alloys Compd.*, 2005, **388**, 274.
98 L. B. Wu and F. Q. Huang, *Z. Kristallogr.–New Cryst. Struct.*, 2005, **220**, 307.
99 L. D. Gulay, O. S. Lychmanyuk, M. Wolcyrz, A. Pietraszko and I. D. Olekseyuk, *J. Alloys Compd.*, 2006, **425**, 159.
100 L. D. Gulay, O. S. Lychmanyuk, I. D. Olekseyuk and A. Pietraszko, *J. Alloys Compd.*, 2006, **422**, 203.
101 M. R. Huch, L. D. Gulay and I. D. Ekseyuk, *J. Alloys Compd.*, 2006, **424**, 114.
102 L. D. Gulay, M. Daszkiewicz, M. R. Huch and A. Pietraszko, *Acta Crystallogr., Sect. E*, 2007, **63**, I187.
103 O. S. Lychmanyuk, L. D. Gulay, I. D. Olekseyuk, J. Stepien-Damm, M. Daszkiewicz and A. Pietraszko, *Pol. J. Chem.*, 2007, **81**, 353.
104 M. Daszkiewicz, L. D. Gulay, O. S. Lychmanyuk and A. Pietraszko, *J. Alloys Compd.*, 2008, **460**, 201.
105 H. Y. Zeng, F. K. Zheng, G. C. Guo and J. S. Huang, *J. Alloys Compd.*, 2008, **458**, 1239.
106 M. Daszkiewicz, L. D. Gulay, O. S. Lychmanyuk and A. Pietraszko, *J. Alloys Compd.*, 2009, **467**, 168.
107 M. Daszkiewicz, L. D. Gulay and O. S. Lychmanyuk, *Acta Crystallogr., Sect. B: Struct. Sci.*, 2009, **65**, 126.

Open Access Article. Published on 22 2024. Downloaded on 18/10/24 08:09:28.
This article is licensed under a Creative Commons Attribution 3.0 Unported Licence.

108 S. P. Guo, G. C. Guo, M. S. Wang, J. P. Zou, G. Xu, G. J. Wang, X. F. Long and J. S. Huang, *Inorg. Chem.*, 2009, **48**, 7059.
109 S. P. Guo, G. C. Guo and J. S. Huang, *Sci. China, Ser. B: Chem.*, 2009, **52**, 16095.
110 O. M. Strok, M. Daszkiewicz, L. D. Gulay and D. Kaczorowski, *J. Alloys Compd.*, 2010, **493**, 47.
111 B. W. Rudyk, S. S. Stoyko and A. Mar, *J. Solid State Chem.*, 2013, **208**, 78.
112 B. W. Liu, H. Y. Zeng, Z. Y. Zhao, F. K. Zheng, G. C. Guo and J. S. Huang, *Chin. J. Struct. Chem.*, 2013, **32**, 1537.
113 B. W. Rudyk, S. S. Stoyko, A. O. Oliynyk and A. Mar, *J. Solid State Chem.*, 2014, **210**, 79.
114 W. L. Yin, Y. G. Shi, B. Kang, J. G. Deng, J. Y. Yao and Y. C. Wu, *J. Solid State Chem.*, 2014, **213**, 87.
115 X. Zhang, W. Chen, D. Mei, C. Zheng, F. Liao, Y. Li, J. Lin and F. Huang, *J. Alloys Compd.*, 2014, **610**, 617.
116 M. Daszkiewicz, O. V. Marchuk, L. D. Gulay and D. Kaczorowski, *J. Alloys Compd.*, 2014, **610**, 258.
117 M. Daszkiewicz, Y. O. Pashynska, O. V. Marchuk, L. D. Gulay and D. Kaczorowski, *J. Alloys Compd.*, 2014, **616**, 243.
118 H. J. Zhao, Synthesis, Crystal and Electronic Structure, and Optical Property of the Quaternary Selenide: $La_3Sb_{0.33}SiSe_7$, *Z. Anorg. Allg. Chem.*, 2015, **641**, 917.
119 O. Strok, M. Daszkiewicz and L. Gulay, *Chem. Met. Alloys*, 2015, **8**, 16.
120 M. Daszkiewicz, Y. O. Pashynska, O. V. Marchuk, L. D. Gulay and D. Kaczorowski, *J. Alloys Compd.*, 2015, **647**, 445.
121 A. K. Iyer, B. W. Rudyk, X. S. Lin, H. Singh, A. Z. Sharma, C. R. Wiebe and A. Mar, *J. Solid State Chem.*, 2015, **229**, 150.
122 A. Choudhury and P. K. Dorhout, *Inorg. Chem.*, 2015, **54**, 1055.
123 A. K. Iyer, W. L. Yin, E. J. Lee, X. S. Lin and A. Mar, *J. Solid State Chem.*, 2017, **250**, 14.
124 N. Zhen, L. Y. Nian, G. M. Li, K. W and S. L. P, *Crystals*, 2016, **6**, 121.
125 Y. Zhou, A. K. Iyer, A. O. Oliynyk, M. Heyberger, Y. Lin, Y. Qiu and A. Mar, *J. Solid State Chem.*, 2019, **278**, 120914.
126 Y. Yang, Y. Chu, B. B. Zhang, K. Wu and S. L. Pan, *Chem. Mater.*, 2021, **33**, 4225.
127 G. Akopov, N. W. Hewage, P. Yox, G. Viswanathan, S. J. Lee, L. P. Hulsebosch, S. D. Cady, A. L. Paterson, F. A. Perras, W. Q. Xu, K. Wu, Y. Mudryk and K. Kovnir, *Chem. Sci.*, 2021, **12**, 14718.
128 L. H. Gao, X. W. Wu, J. J. Xu, X. Y. Tian, B. B. Zhang and K. Wu, *J. Alloys Compd.*, 2022, **900**, 163535.
129 A. J. Craig, J. B. Cho, S. H. Shin, S. H. Ha, S. S. Stoyko, J. I. Jang and J. A. Aitken, *J. Alloys Compd.*, 2022, **910**, 164855.
130 Y. Wang, Y. F. Shi, Y. Lin, Z. Chen and L. T. Li, *Inorg. Chem. Commun.*, 2023, **153**, 110829.
131 J.-X. Zhang, M.-Y. Ran, X.-T. Wu, H. Lin and Q.-L. Zhu, *Inorg. Chem. Front.*, 2023, **10**, 5244.
132 W. Xing, N. Wang, Y. Guo, Z. Li, J. Tang, K. Kang, W. Yin, Z. Lin, J. Yao and B. Kang, *Dalton Trans.*, 2019, **48**, 17620.
133 W. Xing, C. Tang, N. Wang, C. Li, Z. Li, J. Wu, Z. Lin, J. Yao, W. Yin and B. Kang, *Inorg. Chem.*, 2020, **59**, 18452.
134 M. C. Chen, P. Li, L. J. Zhou, L. H. Li and L. Chen, *Inorg. Chem.*, 2011, **50**, 12402.
135 W. Yin, K. Feng, W. Wang, Y. Shi, W. Hao, J. Yao and Y. Wu, *Inorg. Chem.*, 2012, **51**, 6860.
136 W. Yin, W. Wang, L. Bai, K. Feng, Y. Shi, W. Hao, J. Yao and Y. Wu, *Inorg. Chem.*, 2012, **51**, 11736.
137 Q. G. Yue, S. H. Zhou, B. Li, X. T. Wu, H. Lin and Q. L. Zhu, *Inorg. Chem.*, 2022, **61**, 1797.
138 A. Mazurier, S. Jaulmes and M. Guittard, *Acta Crystallogr., Sect. C*, 1987, **43**, 1859.
139 J. J. Xu, K. Wu, Y. Xiao, B. B. Zhang, H. H. Yu and J. H. Zhang, *ACS Appl. Mater. Interfaces*, 2022, **14**, 37967.
140 J. J. Xu, K. Wu, B. B. Zhang, H. H. Yu and J. H. Zhang, *Inorg. Chem. Front.*, 2023, **10**, 2045.
141 H. Y. Zeng, Z. Y. Zhao, S. P. Guo, F. K. Zheng, G. C. Guo and J. S. Huang, *J. Alloys Compd.*, 2012, **514**, 135.
142 J. Xu, Y. Xiao, K. Wu, B. Zhang, D. Lu, H. Yu and H. Zhang, *Small*, 2024, **20**, 2306577.
143 Y. X. Han, C. L. Hu, B. X. Li and J. G. Mao, *Mater. Today Phys.*, 2023, **31**, 100987.
144 P. Wu and J. A. Ibers, *J. Solid State Chem.*, 1993, **107**, 347.
145 M. Usman, M. D. Smith, G. Morrison, V. V. Klepov, W. Zhang, P. S. Halasyamani and H. C. Zur Loye, *Inorg. Chem.*, 2019, **58**, 8541.
146 A. K. Gray, J. M. Knaust, B. C. Chan, L. A. Polyakova and P. K. Dorhout, *Z. Kristallogr.–New Cryst. Struct.*, 2005, **220**, 293.
147 S. P. Guo, H. Y. Zeng, G. C. Guo, J. P. Zou, G. Xu and J. S. Huang, *Chin. J. Struct. Chem.*, 2008, **27**, 1543.
148 D. J. Mei, W. Z. Cao, N. Z. Wang, X. X. Jiang, J. Zhao, W. K. Wang, J. H. Dang, S. Y. Zhang, Y. D. Wu and P. H. Rao, *Mater. Horiz.*, 2021, **8**, 2330.
149 X. Tian, Y. Xiao, B. Zhang, D. Yang and K. Wu, *Mater. Today Phys.*, 2022, **28**, 100885.
150 A. Assoud, K. M. Kleinke and H. Kleinke, *Chem. Mater.*, 2006, **18**, 1041.
151 H. J. Zhao and L. J. Zhou, *Eur. J. Inorg. Chem.*, 2015, **6**, 964.
152 G. G. Guseinov, F. K. Mamedov, I. R. Amiraslanov and K. S. Mamedov, *Z. Kristallogr.*, 1981, **26**, 831.
153 H. J. Zhao and X. A. Zhong, *J. Solid State Chem.*, 2017, **251**, 65.
154 H. Lin, Y. Y. Li, M. Y. Li, Z. Ma, L. M. Wu, X. T. Wu and Q. L. Zhu, *J. Mater. Chem. C*, 2019, **7**, 4638.
155 A. M. Kussainova, L. G. Akselrud, N.-T. Suen, L. Voss, S. Stoyko and S. Bobev, *J. Solid State Chem.*, 2016, **233**, 269.
156 H. J. Zhao, Y. F. Zhang and L. Chen, *J. Am. Chem. Soc.*, 2012, **134**, 1993.
157 M. C. Chen, L. H. Li, Y. B. Chen and L. Chen, *J. Am. Chem. Soc.*, 2011, **133**, 4617.
158 H. J. Zhao, *Z. Anorg. Allg. Chem.*, 2015, **642**, 56.
159 Y. Wang, X. C. Zou, X. Feng, Y. F. Shi and L. M. W, *J. Solid State Chem.*, 2017, **245**, 110.
160 H. J. Zhao, *J. Solid State Chem.*, 2016, **237**, 99.
161 Y. Wang, H. J. Zhao, Y.-F. Shi, P. F. Liu, X. C. Zou and Y. R. Ren, *Chin. J. Struct. Chem.*, 2017, **36**, 1465.


© 2024 The Author(s). Published by the Royal Society of Chemistry

Open Access Article. Published on 22 2024. Downloaded on 18/10/24 08:09:28.
This article is licensed under a Creative Commons Attribution 3.0 Unported Licence.

162 W. Yin, A. K. Iyer, C. Li, J. Yao and A. Mar, *J. Alloys Compd.*, 2017, **710**, 424.
163 J. Hunger, M. Borna and R. Kniep, *J. Solid State Chem.*, 2010, **183**, 702.
164 M. Borna, J. Hunger and R. Kniep, *Z. Kristallogr.–New Cryst. Struct.*, 2010, **225**, 223.
165 M. Borna, J. Hunger and R. Kniep, *Z. Kristallogr.–New Cryst. Struct.*, 2010, **225**, 225.
166 M. Borna, J. Hunger, A. Ormeci, D. Zahn, U. Burkhardt, W. C. Cabrera, R. C. Gil and R. Kniep, *J. Solid State Chem.*, 2011, **184**, 296.
167 L. S. Breton, G. Morrison, M. R. Lacroix, P. S. Halasyamani and H. C. Zur Loye, *Chem. Commun.*, 2022, **58**, 7992.
168 Y. X. Han, C. L. Hu, Z. Fang, Q. Q. Chen, B. X. Li, Y. Lin and J. G. Mao, *J. Mater. Chem. C*, 2022, **10**, 12556.
169 Y. X. Han, C. L. Hu and J. G. Mao, *Small*, 2024, **20**, 2305828.
170 W. Brockner and R. Becker, *Z. Naturforsch. A*, 1987, **42**, 511.
171 X. Huang, S. H. Yang, X. H. Li, W. Liu and S. P. Guo, *Angew. Chem., Int. Ed.*, 2022, **61**, e202206791.
172 Z. X. Chen, C. Y. Zhao, X. H. Li, W. D. Yao, W. Liu and S. P. Guo, *Small*, 2023, **19**, 2206910.
173 F. Lin, M. Luo, R. Wang, X. Che and F. Huang, *CrystEngComm*, 2021, **23**, 2133.
174 A. Cicirello, A. Swindle and J. Wang, *CrystEngComm*, 2023, **25**, 6354.
175 D. H. Kang, F. Ledderboge, H. Kleinke and T. Schleid, *Z. Anorg. Allg. Chem.*, 2015, **641**, 322.
176 Y. Chi, H. G. Xue and S. P. Guo, *Inorg. Chem.*, 2020, **59**, 1547.
177 S. P. Guo, G. C. Guo, M. S. Wang, J. P. Zou, H. Y. Zeng, L. Z. Cai and J. S. Huang, *Chem. Commun.*, 2009, **29**, 4366.
178 H. J. Zhao, P. F. Liu and L. M. Wu, *Dalton Trans.*, 2021, **50**, 2075.
179 H. J. Zhao, H. D. Yang, P. F. Liu and H. Lin, *Cryst. Growth Des.*, 2022, **22**, 1437.
180 Z. T. Lu, W. J. Fan, Z. Q. Wang, N. Gu, Z. H. Yue, H. G. Xue and S. P. Guo, *Inorg. Chem.*, 2020, **59**, 7905.
181 M. Yang, W. D. Yao, W. Liu and S. P. Guo, *Chem. Commun.*, 2023, **59**, 3894.
182 C. Boyer-Candalen, A. Meerschaut and P. Palvadeau, *Mater. Res. Bull.*, 2000, **35**, 1593.
183 H. Kabbour, L. Cario, C. Deudon and A. Meerschaut, *Acta Crystallogr., Sect. E*, 2003, **59**, i101.
184 S. Altmannshofer and D. Johrendt, *Z. Anorg. Allg. Chem.*, 2008, **634**, 1361.
185 X. Lian, Z. T. Lu, W. D. Yao, S. H. Yang, W. Liu, R. L. Tang and S. P. Guo, *Inorg. Chem.*, 2021, **60**, 10885.
186 M. Y. Ran, S. H. Zhou, W. B. Wei, B. X. Li, X. T. Wu, H. Lin and Q. L. Zhu, *Small*, 2023, **19**, 2300248.
187 N. Zhang, X. Huang, W. D. Yao, Y. Chen, Z. R. Pan, B. Li, W. Liu and S. P. Guo, *Inorg. Chem.*, 2023, **62**, 16299.
188 D. Mei, W. Yin, L. Bai, Z. Lin, J. Yao, P. Fu and Y. Wu, *Dalton Trans.*, 2011, **40**, 3610.
189 K. Wu, Z. Yang and S. Pan, *Chem. Mater.*, 2016, **28**, 2795.
190 H. Chen, P. Liu, B. Li, H. Lin, L. Wu and X.-T. Wu, *Dalton Trans.*, 2018, **47**, 429.
191 Y. Yang, K. Wu, X. Wu, B. Zhang and L. Gao, *J. Mater. Chem. C*, 2020, **8**, 1762.
192 G. Li, Z. Yang, J. Li and S. L. Pan, *Chem. Commun.*, 2020, **56**, 11565.
193 D. Desaintg, P. Laruelle and J. Flahaut, *C. R. Acad. Sci., Ser. C*, 1968, **267**, 1029.
194 M. Patrie and M. Guittard, *C. R. Acad. Sci., Ser. C*, 1969, **268**, 1136.
195 Y. Zhang, D. Mei, Y. Yang, W. Cao, Y. Wu, J. Lu and Z. Lin, *J. Mater. Chem. C*, 2019, **7**, 8556.
196 Y. Guo, F. Liang, W. Yin, Z. Li, X. Luo, Z.-S. Lin, J. Yao, A. Mar and Y. Wu, *Chem. Mater.*, 2019, **31**, 3034.
197 Y.-J. Lin, B.-W. Liu, R. Ye, X.-M. Jiang, L.-Q. Yang, H.-Y. Zeng and G.-C. Guo, *J. Mater. Chem. C*, 2019, **7**, 4459.
198 M. Yan, Z.-D. Sun, W.-D. Yao, W. Zhou, W. Liu and S.-P. Guo, *Inorg. Chem. Front.*, 2020, **7**, 2451.
199 H.-D. Yang, M.-Y. Ran, S.-H. Zhou, X.-T. Wu, H. Lin and Q.-L. Zhu, *Chem. Sci.*, 2022, **13**, 10725.
200 Y.-N. Li, Z.-X. Chen, W.-D. Yao, R.-L. Tang and S.-P. Guo, *J. Mater. Chem. C*, 2021, **9**, 8659.
201 Q. Q. Liu, X. Liu, L. M. Wu and L. Chen, *Angew. Chem., Int. Ed.*, 2022, **61**, e202205587.
202 M.-Y. Ran, S.-H. Zhou, W.-B. Wei, B.-X. Li, X.-T. Wu, H. Lin and Q.-L. Zhu, *Small*, 2024, **20**, 2304563.
203 H. Lin, Y. Liu, L. J. Zhou, H. J. Zhao and L. Chen, *Inorg. Chem.*, 2016, **55**, 4470.
204 H. Lin, H. Chen, Y. J. Zheng, J. S. Yu and L. M. Wu, *Dalton Trans.*, 2016, **45**, 17606.
205 M.-Y. Ran, Z. Ma, X.-T. Wu, H. Lin and Q.-L. Zhu, *Inorg. Chem. Front.*, 2021, **8**, 4838.
206 Y. T. Yang and J. A. Ibers, *J. Solid State Chem.*, 2000, **149**, 384.
207 M. C. Chen, L. M. Wu, H. Lin, L. J. Zhou and L. Chen, *J. Am. Chem. Soc.*, 2012, **134**, 6058.
208 M.-Y. Li, B. Li, H. Lin, Z. Ma, L.-M. Wu, X.-T. Wu and Q.-L. Zhu, *Chem. Mater.*, 2019, **31**, 6268.
209 M.-M. Chen, Z. Ma, B.-X. Li, W.-B. Wei, X.-T. Wu, H. Lin and Q.-L. Zhu, *J. Mater. Chem. C*, 2021, **9**, 1156.
210 Y. Xiao, M. M. Chen, Y. Y. Shen, P. F. Liu, H. Lin and Y. Liu, *Inorg. Chem. Front.*, 2021, **8**, 2835.
211 M. Yan, H.-G. Xue and S.-P. Guo, *Cryst. Growth Des.*, 2021, **21**, 698.
212 C. Liu, S.-H. Zhou, Y. Xiao, C. Zhang, H. Lin and Y. Liu, *J. Mater. Chem. C*, 2021, **9**, 15407.
213 X.-H. Li, Z.-H. Shi, M. Yang, W. Liu and S.-P. Guo, *Angew. Chem., Int. Ed.*, 2022, **61**, e202115871.
214 M.-M. Chen, S.-H. Zhou, W. Wei, M.-Y. Ran, B. Li, X.-T. Wu, H. Lin and Q.-L. Zhu, *ACS Mater. Lett.*, 2022, **4**, 1264.
215 J. K. Harada, N. Charles, K. R. Poeppelmeier and J. M. Rondinelli, *Adv. Mater.*, 2019, **31**, 1805295.
216 H. Kageyama, K. Hayashi, K. Maeda, J. P. Attfield, Z. Hiroi, J. M. Rondinelli and K. R. Poeppelmeier, *Nat. Commun.*, 2018, **9**, 772.
217 Y. Pan, S.-P. Guo, B.-W. Liu, H.-G. Xue and G.-C. Guo, *Coord. Chem. Rev.*, 2018, **374**, 464.
218 R. Wang, F. Liang, F. Wang, Y. Guo, X. Zhang, Y. Xiao, K. Bu, Z. Lin, J. Yao, T. Zhai and F. Q. Huang, *Angew. Chem., Int. Ed.*, 2019, **58**, 8078.

Open Access Article. Published on 22 2024. Downloaded on 18/10/24 08:09:28.
This article is licensed under a Creative Commons Attribution 3.0 Unported Licence.

219 M. Y. Ran, Z. J. Ma, H. Chen, B. X. Li, X. T. Wu, H. Lin and Q. L. Zhu, *Chem. Mater.*, 2020, **32**, 5890.
220 H. Chen, Y. Y. Li, B. X. Li, P. F. Liu, H. Lin, Q. L. Zhu and X. T. Wu, *Chem. Mater.*, 2020, **32**, 8012.
221 H. Yan, Y. Matsushita, K. Yamaura and Y. Tsujimoto, *Angew. Chem., Int. Ed.*, 2021, **60**, 26561.
222 Y.-F. Shi, Z. Ma, B.-X. Li, X. Wu, H. Lin and Q.-L. Zhu, *Mater. Chem. Front.*, 2022, **6**, 3054.
223 Y. F. Shi, S. H. Zhou, B. Li, Y. Liu, X. T. Wu, H. Lin and Q. L. Zhu, *Inorg. Chem.*, 2023, **62**, 464.
224 Q.-G. Yue, W.-B. Wei, H. Chen, X.-T. Wu, H. Lin and Q.-L. Zhu, *Dalton Trans.*, 2020, **49**, 14338.
225 M.-Y. Ran, S.-H. Zhou, B.-X. Li, W.-B. Wei, X.-T. Wu, H. Lin and Q.-L. Zhu, *Chem. Mater.*, 2022, **34**, 3853.
226 H.-D. Yang, S.-H. Zhou, M.-Y. Ran, X.-T. Wu, H. Lin and Q.-L. Zhu, *Inorg. Chem.*, 2022, **61**, 15711.
227 J. Wang, Y. Cheng, H. Wu, Z. Hu, J. Wang, Y. Wu and H. Yu, *Angew. Chem., Int. Ed.*, 2022, **61**, e202201616.
228 H.-D. Yang, S.-H. Zhou, M.-Y. Ran, X.-T. Wu, H. Lin and Q.-L. Zhu, *Inorg. Chem. Front.*, 2023, **10**, 2030.
229 Y. F. Shi, X. F. Li, Y. X. Zhang, H. Lin, Z. J. Ma, L. M. Wu, X. T. Wu and Q. L. Zhu, *Inorg. Chem.*, 2019, **58**, 6588.
230 M. Y. Li, Y. X. Zhang, H. Lin, Z. J. Ma, X. T. Wu and Q. L. Zhu, *Dalton Trans.*, 2019, **48**, 17588.
231 S.-H. Zhou, M.-Y. Ran, W.-B. Wei, A.-Y. Wang, X.-T. Wu, H. Lin and Q.-L. Zhu, *Inorg. Chem. Front.*, 2023, **10**, 5997.
232 X. Chen, S.-H. Zhou, C. Zhang, H. Lin and Y. Liu, *Chem. Commun.*, 2023, **59**, 12124.
233 Y.-F. Shi, S.-H. Zhou, P.-F. Liu, X.-T. Wu, H. Lin and Q.-L. Zhu, *Inorg. Chem. Front.*, 2023, **10**, 4425.
234 S. P. Guo, C. Yang, B. W. Liu and G. C. Guo, *Dalton Trans.*, 2016, **45**, 10459.
235 Z. D. Sun, Y. Chi, H. G. Xue and S. P. Guo, *Inorg. Chem. Front.*, 2017, **4**, 1841.
236 S. S. Han, W. D. Yao, S. X. Yu, Y. L. Sun, A. H. Gong and S. P. Guo, *Inorg. Chem.*, 2021, **60**, 3375.


© 2024 The Author(s). Published by the Royal Society of Chemistry